The effect of Electro Spark Deposition on the microstructure and mechanical properties of IN718

by

Lorenzo Marzari Felix

A thesis
presented to the University of Waterloo
in fulfillment of the
thesis requirement for the degree of
Master of Applied Science
in
Mechanical and Mechatronics Engineering

Waterloo, Ontario, Canada, 2018

Author's declaration

I hereby declare that I am the sole author of this thesis. This is a true copy of the thesis, including any required final revisions, as accepted by my examiners.

I understand that my thesis may be made electronically available to the public.

Abstract

The Electro Spark Deposition is a technique of continuing interest to repair or coat the surface of expensive components used in the aerospace industry. A potential use for this technique is to repair damaged turbine blades made with nickel-based superalloys, such as IN718.

Nickel-based superalloys are susceptible to hot cracking and post weld heat treatment cracking during conventional processes, due to the high heat input that contributes to issues mainly observed in the heat affected zone of the components. An interesting approach to reduce thermal issues in nickel-based superalloys is to reduce the heat input during welding or posterior treatments. In this case, the use of the ESD technique to repair expensive parts made with nickel-based superalloys is a possibility, since this process has the advantage to generate minimal heat input onto the substrate.

In order to better understand the inherent defects of this method and the microstructure and properties achieved through the ESD process, a systematic study of the effects of the main variables in this process is a necessity, including but not limited to the voltage, capacitance and spark frequency.

In this work, IN718 deposited using ESD with different pulse energy and frequency, achieved by varying the voltage, capacitance and pulse frequency, was systematically investigated in terms of its microstructure, microhardness and tensile properties. It has been observed that the increasing pulse energy and frequency in the ESD process promotes the formation of internal voids and intermetallic phases that may be undesirable in the process of repairing or coating of components. The presence of intermetallic phases in a certain amount and distribution is believed to increase the susceptibility for cracking of the deposited layers. Tensile samples repaired with conditions that present less internal defects showed ductility closer to the ductility observed for the parent material.

Acknowledgements

During all my life and my endeavors, I had support and inspiration from my mother, Landis Maria Marzari. Her tenacity and courage to face life is what propels me towards my dreams. There are no words that can express all my gratitude for her. Together with my siblings, Luciane and Lucas, we have passed through tough times, and encouraged each other to move forward.

To my wife, Taisa, who was always beside me during this path.

To Professor Norman Zhou, for the opportunity to study at the University of Waterloo.

To Charles Chi Fong (Charles) Kwan. His commitment and tremendous help during this project certainly guided me to expand my knowledge. I will always be grateful for our invaluable discussions.

I would like to thank Huys Industries Limited, in special to Nigel Scotchmer for the assistance and Stephen Peterkin for his greatly help.

Finally, I would like to thank all the members of the CAMJ group and the University of Waterloo that assisted me during my time in this University.

Table of Contents

List of Figures

List of Tables

Quant à vous, Morrel, voici tout le secret de ma conduite envers vous : il n'y a ni bonheur ni malheur en ce monde, il y a la comparaison d'un état à un autre, voilà tout. Celui-là seul qui a éprouvé l'extrême infortune est apte à ressentir l'extrême félicité. Il faut avoir voulu mourir, Maximilien, pour savoir combien il est bon de vivre.

Alexandre Dumas, Le Comte de Monte-Cristo

1. Chapter 1 – Introduction

1.1 Background

Electro-Spark Deposition (ESD) is a process initially used as a micro-welding technique whereby pulsed arcs are generated between a moving electrode and the base metal. As a result of the pulse arcs, material from the electrode is ejected in the form of molten droplets towards the substrate, which have been heated up to a partially molten state due to the arcs, forming a thin alloying zone with the base material [1, 2]. The deposition of the electrode materials often takes on a macrostructure commonly referred to as a splat. Due to the nature of the ESD processing leading to the deposition of the electrode material onto the substrate, it further evolved into a deposition-based coating process which may be used to increase wear or corrosion resistance of the substrate or for dimensional restoration [3].

The ESD technique has many advantages, including but not limited to the excellent coating adhesion of the coating to the substrate and the minimal effect the process has on the microstructure of the base metal [4, 5]. The short duration of the arcing processing combined with the intermittent contact between the electrode and the substrate results in an extremely low heat input, thus leading to a minimal alteration to the microstructure of the base metal. Consequently, the ESD process generally result in a small or nearly non-existent Heat Affected Zone (HAZ), thus minimizing changes in the microstructure and mechanical properties of the substrate [4, 5]. Although the ESD process offers many benefits, the process also has some limitations regarding its applications, such as the low deposition rate and the consistency of coating properties [2, 3].

The aerospace industry widely uses superalloys in aircrafts engines, mainly in high pressure and high temperature sections of the turbine. The temperature and pressure profile presented in Figure 1.1 shows that the hot section of the turbine, comprising the combustion chamber, high and low-pressure turbine and nozzle, endures the maximum temperature combined with high pressure in an engine.
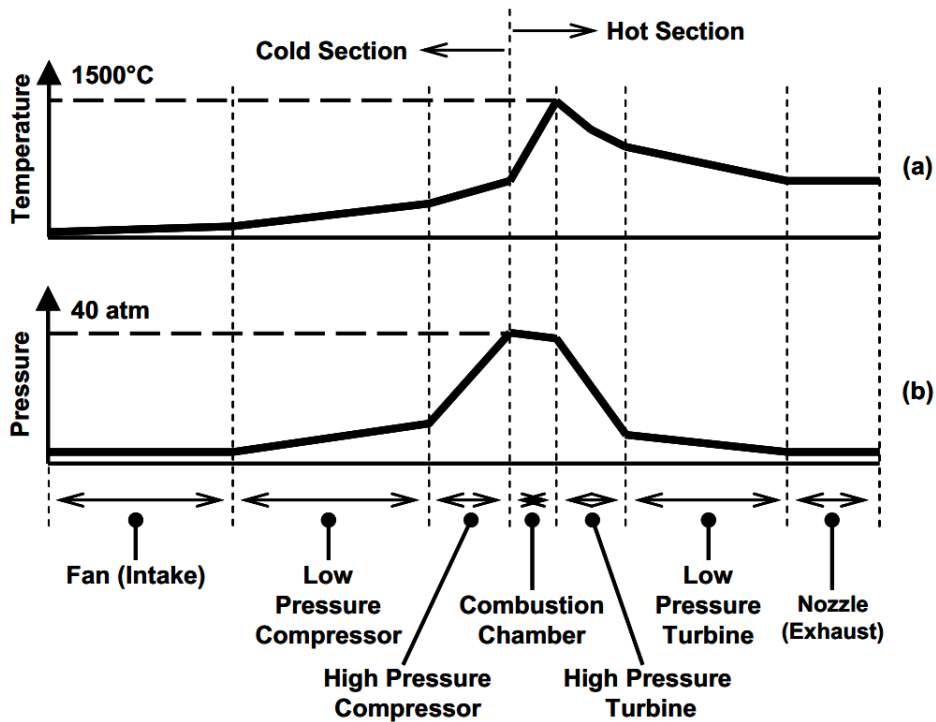
Figure 1.1: Temperature and pressure profiles in a common turbine engine [6].

Components manufactured with Ni-based superalloys present excellent properties at high temperature, as resistance to creep, corrosion and oxidation [6, 7]. The precipitation-hardening Ni-based superalloys, like Inconel 718 (IN718), are being used in high temperature applications due to their excellent mechanical strength and resistance to degradation in oxidizing and corrosive environment [8]. Figure 1.2 shows where the nickel alloys are used in an engine, mainly in the hot-section of the engine.
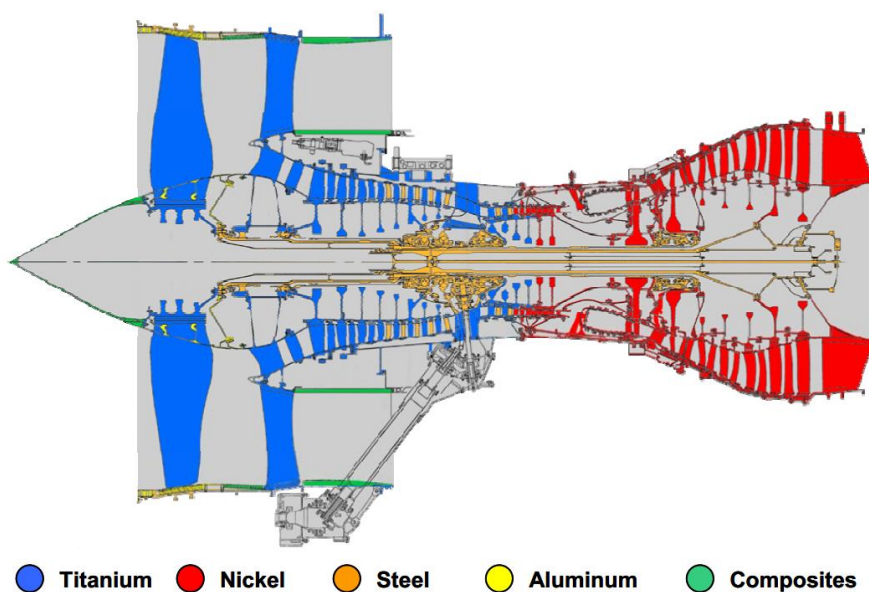
Figure 1.2: Materials commonly observed in a turbine [6].

2

Turbine blades manufactured with superalloys may present cracks nucleated from different sources that may lead the component to failure [9, 10]. The components made with superalloys have a high manufacturing and material costs, and simple replace a damaged component may not be an economic advantage. Repairing damaged pieces, using a welding process, is a possibility to reduce operational costs [1].

Ni-based superalloys are susceptible to hot cracking during welding processes and post weld heat treatment cracking [11]. The presence of hot cracks occurs mainly in the HAZ of the material, when relatively high heat inputs are used. Controlling heat input minimizes the occurrence of HAZ fissuring [12]. More recently, the ESD process has been adopted to carry out reparair of engineering components. The advantages of the ESD process is especially beneficial to the reparation of turbine blades made of Ni based superalloys, such as IN718. The ESD technique produces almost no HAZ and has a low effect on the base metal, thus this technique is attractive for repairing of advanced precipitation hardened Ni-based superalloys for application at high temperatures, like IN718 [5, 13].

Having in mind the potential applications and challenges to use ESD to deposit and possibly repair Ni-based superalloys components, understand the microstructure and mechanical properties of ESD repaired samples is a necessity. This work aims to investigate the effect of pulse energy and the variance of pulse frequency on the microstructure and properties of ESD deposited IN718, evaluating the effects of the parameters on the formation of defects, the microstructure evolution and mechanical properties of IN718 deposited through this microwelding technique.

1.2   Objective

The objective of this thesis is to understand the effects of the pulse energy and pulse frequency on the microstructure and properties of the Ni-based superalloy IN718. The detailed objectives include:

1) A comprehensive examination of the internal defects and discontinuities of ESD depositions made with different pulse energy and pulse frequency.

2) The effect of different pulse energy and frequency on the roughness of ESD depositions and its relations to the internal defects.

3) The microstructure evolution of the ESD deposited IN718 using different pulse energy and pulse frequency.

4) The effects of the volume fraction of defects on the tensile properties of ESD repaired IN718.

1.3   Thesis outline

The literature review is presented, in chapter 2, as the first step to introduce the ESD process to the reader and researcher of this work. In this section, the reader firstly finds a comprehensive description of this process and the applications, as well as advantages and shortcomings of the technique. The ESD equipment and spark formation are indeed described in this section. Superalloys and its features are here presented, as well as the microstructure and properties aspects of ESD repaired materials. In the end of the section, the material transfer and building-up mechanism during ESD process are presented.

The materials and methods section, in chapter 3, describe the ESD equipment, the materials used, experimental conditions for the depositions, performance testing and techniques that were used to conduct the investigation of the data.

After that, in the chapter 4 of this work, mechanisms are proposed and discussed to explain the formation of defects during ESD depositions made with different pulse energies and pulse frequency.

Subsequently, the microstructure evolution and the formation of intermetallic segregation are displayed and discussed in the chapter 5. In the same chapter, the mechanical properties of the ESD repaired IN718 are presented and discussed, in addition to correlations made with the results presented in chapter 4.

Finally, the conclusions and the recommendations for future work are proposed at the end of this thesis.

2. Chapter 2 – Literature Review

2.1 Electro-spark deposition as a micro-welding process

ESD is a technique for surface modification; therefore, physical and chemical properties of metal surfaces are changed during this process. The process is a low heat-input, high energy density, micro-welding process, included in the family of the rapid solidification processes, having little effect on the substrate properties [14, 3].

One of the earliest known reference to the effect of spark treatments on surface properties date back to 1924, where Rawdon, *apud* Johnson and Sheldon [15], discovered that iron sparked with a similar electrode became extremely hard. Rawdon showed that the increased hardness of the iron surface was due to the formation of martensite during the rapid quenching of the spark-heated surface [15].

The study of ESD grew substantially during the second half of the twentieth century, with practical applications developed in Eastern Europe [15]. The limitations intrinsically connected to the process restrain a widely usage of this technique to increase desired properties and behaviors of metallic components [2].

The core of the ESD method consists in the erosion of electrode and substrate as a result of the electric discharge between them in a gaseous environment, with subsequent mass transfer from one of them to the other [16]. A rotating electrode is applied as the anode in the process. The substrate is the cathode, having significantly larger size and surface area. The electrode and substrate must be electrically conductive. The energy stored in capacitors is discharged through a sequence of short sparks that take place between the electrode and the substrate. Following spark discharge, small portions of the tip of electrode and the substrate are melted [2, 16]. Some of the melted material from the tip of the electrode is transferred to the surface of the substrate, mixing materials in a high-pressure and high-temperature discharging micro-zone, forming a molten pool that usually solidifies in the form of a splash or splat [16, 17, 18]. Figure 2.1 represents the formation of a single splat in an ESD deposition.
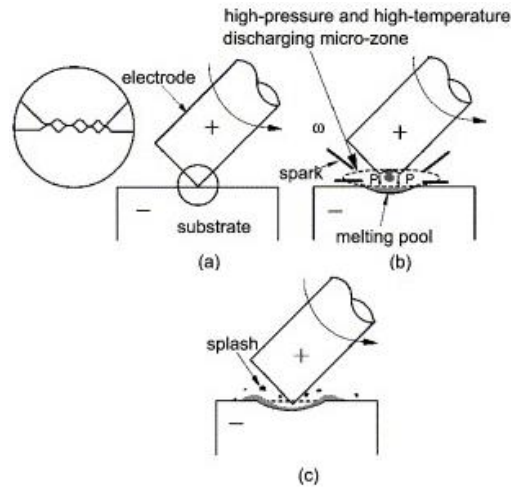
Figure 2.1: The formation of a single splash or splat in an ESD deposition [17].

ESD deposits involve the formation of individual splats which are connected together by metallurgical bonding, forming a thin alloying zone with the base material [2, 18]. Individual splats are characterized by the topographic morphology observed in Figure 2.2 (a). The material distribution is uneven during the formation of an individual splat, with a valley in the center and built up of material on the sides. A cross-section of a splat can be observed in Figure 2.1 (c), where is possible to observe the formation of a cavity in the middle of the splat and the solidified material on the periphery of the crater. The ESD layer consists of different stacked splats positioned side by side, and as the process of deposition continues, a homogeneous and fine microstructure within the processed region is achieved, as observed in Figure 2.2 (b) [5].
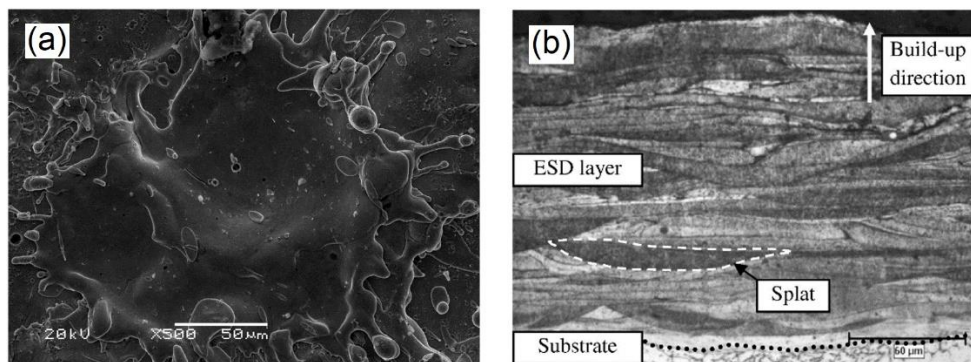
Figure 2.2: (a) Top surface of an individual splat, showing its topographic morphology. (b) ESD layer of Nickel-based superalloy, showing disposition of a splat and the interface deposition-substrate [5].

2.2   Applications of ESD

There are two major applications of ESD: for repairing of damaged pieces and surface-modification. For the first case, the ESD technique is applied to repair pieces that present specific types of flaws, like cracks or eroded areas. For the occasion of surface-modification, the ESD method is applied to obtain the required properties, like wear and corrosion resistance [3]. Table 2.1 lists different coating applied by the ESD process to acquire different properties and restoration.

Table 2.1: ESD coating applied for different materials [19].

Wear Resistance Coating	Corrosion Resistance Coating	Build-up or Special Surface Modification
Hard carbides[a] of: W, Cr, Ti, Ta, Hf, Mo, Zr, V, Nb	Stainless steels, Hastelloys[b], Inconels[b], Monels[b]	Ni-based and Co-based super alloys
Hardfacing alloys: Stellites[b], Tribaloys[b], Colmonoys[b], etc	Aluminides of: Fe, Ni, and Ti	Refractory Alloys (W, Ta, Mo, Nb, Re, Hf)
Borides of: Cr, Ti, Zr, and Ta	FeCrAlY, NiCrAlY, CoCrAlY	Noble metals (Au, Pt, Ag, Pd, Ir)
Intermetallics and Cermets	Al and Al Bronze Alloys	Other Alloys (Fe, Ni, Cr, Co, Al, Cu, Ti, V, Sn, Er, Zr, Zn)

(a) With metal binders, usually 5-15% Ni or Co

(b) Trademarks: Hastelloy – Haynes International, Kokomo, IN

Inconel & Monel – International Nickel Co, Huntington, WV

Stellite & Tribaloy – Deloro-Stellite Co., Goshen, IN

Colmonoy – Wall Colmonoy Corp., Detroit, MI

ESD is commonly used in aerospace applications, finding applicability in the surface treatments for improving wear, erosion, and corrosion resistance. Restoration and recovery of high values parts, such as turbine components made in nickel-based superalloys is a possibility for the ESD process [19]. Figure 2.3 shows a single crystal turbine blade before ESD repairing in (a) and after repairing in (c). This component presented thermal fatigue cracks, and after the removal of these flaws by grinding, the piece was restored by ESD using the same superalloy as the base metal.
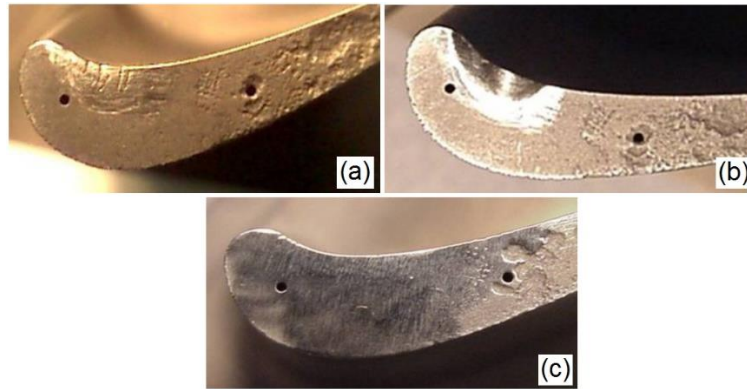
Figure 2.3: Turbine blade restored by ESD: a) original piece with thermal fatigue cracks, b) defects removed by grinding, c) restored piece after finishing [19].

2.3   Advantages and limitations of the ESD process

The ESD process offers a wide number of benefits. One of the biggest advantages of this process is the extremely low heat input, and changes in the metallurgical structure or distortion of the substrate are negligible. The ESD technique is appropriate to be applied in materials that may suffer sensitizing during welding. The rapid quench rate observed in ESD deposition results in an extremely fine-grained coating structure. This fine microstructure is believed to contribute to the excellent erosion resistance of the ESD coatings [15].

ESD can be applied nearly for all metals and cermets, a single metal-ceramic bulk material. This applicability is regarded as one of the major advantages of this micro-welding process, though the requirements for all depositions consist of an electrically conductive substrate and electrode [15, 16, 20].

Although ESD is relevant and possesses many advantages, it brings a range of limitations. A major disadvantage of the process is the inability to produce rapid deposition rate. Several process variable are believed to influence the deposition rate of the ESD operation. The optimization of the process variables may increase depositions rate and weld quality [3]. Variables affecting coating properties, structure or process efficiency of the ESD technique are presented in Table 2.2. A change in any of these parameters can result in an alteration of the characteristics of deposited layers [15].

8

Table 2.2: Process variables of ESD [3, 15].

Electrode	Electrical	Substrate	Environment	Other
Material	Spark energy	Material	Gas composition	Spark time per unit
Geometry	Voltage	Surface finish	Flow rate	area
Motion	Current	Cleanliness	Flow geometry	Number of passes
Speed	Capacitance	Temperature	Temperature	Overlap of passes
Contact force	Pulse duration	Geometry		
Orientation (relative	Inductance	Roughness		
to workpiece)	Spark frequency			

The ESD depositions depends on a variety of factors, most of them presented in Table 2.2. For example, the contact force will affect the stability of the arc by controlling the gap between the rotating electrode and the stationary substrate. If the pressure is too high, no gap will form during the discharge, suppressing the transfer of material. If the pressure is too low, the electrode will not be able to short with the substrate, avoiding the formation of an arc [3].

The material and the surface finishing of the substrate are also factors that influence the quality of the ESD depositions. It is easier to deposit onto harder materials, and soft materials tend to erode and require a better determination of parameters to avoid erosion [3]. High surface roughness impacts the quality of ESD deposition since irregular contact surfaces may change discharge conditions, generating harmful transient arcs with energy transfer, spot localization and electrode overheating. These undesirable effects undermine efficient and regular depositions due to its influence in coating discontinuity, spatter layers and crater erosion [2].

The environment where an ESD deposition is performed affects the quality of the deposition. Usually, a shielding atmosphere is used in ESD deposition, typically argon is used as shielding gas to inhibit atmospheric contamination of the deposit [3].

Indeed, the ESD process presents a vast range of advantages and limitations, and these features are summarized in Table 2.3.

Table 2.3: Advantages and limitations of the ESD technique [3, 15].

Advantages		Limitations	
Metallurgically bonded coated	Special properties due to rapid solidification	Limited coating thickness	Both substrate and coating material must be electrically conductive
Low effect in the substrate due to low heat input	Little substrate preparation	Extensive optimization of coating parameters may be required for some applications	Clean surface is required
Operators easily trained	Portable equipment and process		
Applicable to complex shapes	Can apply nearly all metals and cermets		

2.4 ESD equipment and electrical features

2.4.1 ESD equipment

ESD equipment consist of two main components: the power source and a handheld torch.

The power source consists of a direct current (DC) rectifier and discharge circuit. Most of the electrical process variables in the ESD process are controlled by the power source, like the charging voltage, capacitance and discharge frequency. The DC rectifier converts alternate current (AC) to DC which is used to charge up a series of capacitors. The discharge of the capacitors is controlled by a resistor capacitor (R-C) or by a microprocessor [3, 19].

The electrode holder, also known as torch, is designed to allow a safe energizing of the consumable electrode during operation. The torch body consist of inner metallic parts, to provide mechanical stability and conductivity, and outer nonconductive material to avoid the risk of electrical shock. The electrode, commonly round to facilitate electrode rotation, is usually held by metallic collets which allow the electrode to have the required movement to produce the sparks in the ESD process. The torch may also be designed to apply shielding gas to the process during operation

[3]. A schematic representation of the ESD equipment and the electrospark deposition is respectively illustrated in Figure 2.4(a) and (b).
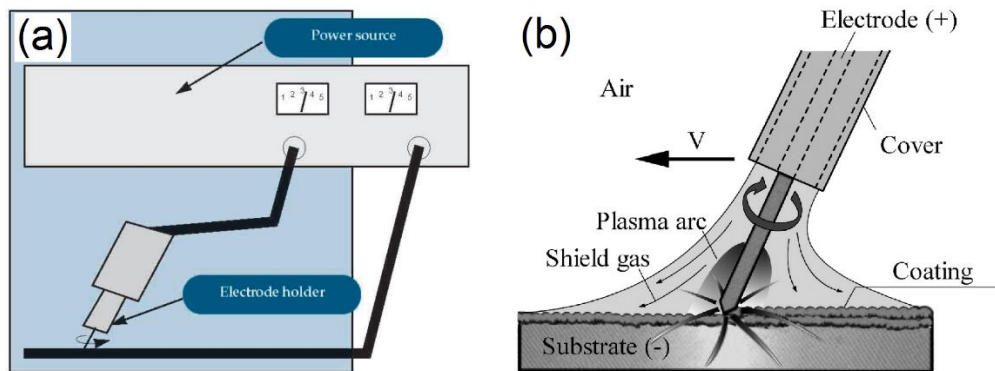
Figure 2.4: Schematic showing the main components of the ESD equipment in (a) [3], and the ESD process in (b) [21].

2.4.2 Formation of sparks during discharge in the ESD process

In the ESD process, the spark is triggered by a contact discharge between the rotating electrode and the base metal. The formation of the spark may theoretically be divided in three distinct phases, as described in Figure 2.5. The first phase observed is the pre-breakdown phase, see Figure 2.5(a), when a discharge current of several Amperes flows through the anode to the cathode, when they come in short-circuit at some contacting sites like protrusions or tips. When the contact between the rotating electrode and the stationary base metal is broken, there is the creating of a micro-gap, producing a high pressure and high temperature spark plasma, in a stage called breakdown phase, as shown in Figure 2.5(b). At the end of the discharge phase, in a stage defined as the post-breakdown phase, plasma pressure collapses, and small molten pieces of the electrode are ejected onto the surface of the substrate and attracted at high velocity mainly towards high field zones like protuberances, where electrostatic forces prevail [2]. The post-breakdown phase is schematically presented in Figure 2.5(c).
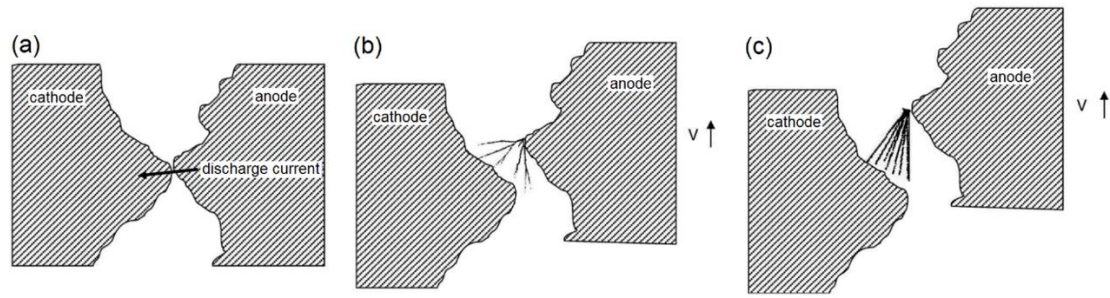
Figure 2.5: Schematic illustration of the ESD discharge phases: (a) pre-breakdown phase, (b) breakdown phase, (c) post-breakdown phase, adapted from reference [2].

A schematic illustration of the discharge phases in the ESD process is observed in Figure 2.6. After the completely charge of the capacitors, the flow of current occurs when there is a point or multiple points of contact, initiating the phase 1 or pre-breakdown phase. As the bank of capacitors is discharged, the current increases, reaching a maximum when the spark breakdown occurs (phase 2). In the end of the spark (phase 3 or post-breakdown phase), the mass transfer takes place with subsequently scattering of molten material.
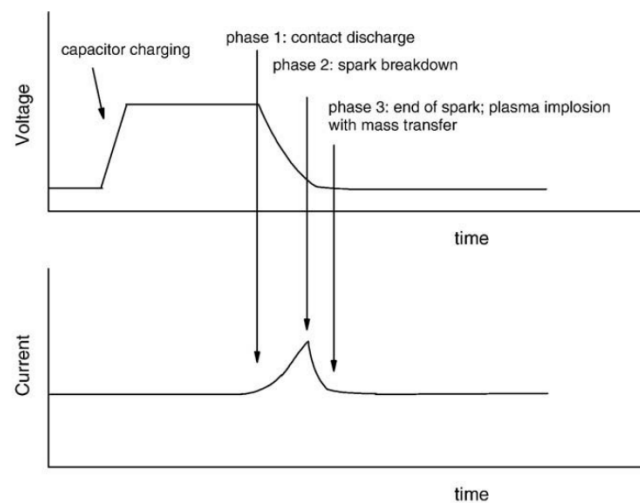
Figure 2.6: Schematic illustration showing the variation of voltage and current in function of time during the discharge phases of the ESD process [2].

2.4.3 Pulse energy in the ESD process

For ESD in air, for a given pair of electrode and substrate, mass transfer depends only on electrical parameters of pulses, or pulse energy [16]. The spark pulse energy (E) in joules (J) can be determined using Equation (1):

$$E = \frac{CV^2}{2}$$
<div align="right">Equation (1)</div>

where C is the capacitance in Farad (F) and V is the voltage in Volts (V) [21, 1, 22].

The energy of each pulse in the ESD process is typically on the order of 0.1-5 Joules, since the capacitance employed is in the order of micro-farads (µF) and the voltages employed are normally on the order of 50-200 volts [23]. The low pulse energy of the ESD process, combined with the small amount of deposited material and the short pulse duration (1-10 µs), induces extremely high cooling rates, on the order of 10^5 to 10^6 K/s [18, 1, 22].

2.5   Superalloys

Superalloys may be face-centered cubic (FCC) austenitic structure of cobalt, iron-nickel, and nickel-based alloys, commonly used in high temperature service, with temperatures above approximately 540 °C (1000 °F) [12, 24].

The properties of the superalloys can be controlled by adjustments in composition and by processing (including heat treatment), and excellent elevated-temperature strengths are available in finished products [12].

Although the intrinsic properties of these alloys allow them to work at high temperatures, the physical metallurgy of these systems is extremely complex, as well as the compositions of these alloys [25]. Phases commonly observed and the role of the alloying elements in the superalloys, as well as features observed in the nickel-based superalloys are discussed in the sequence.

2.5.1   Phases and the role of alloying elements in superalloys

The superalloys are strengthened by two major mechanisms: precipitation of phases and solid-solution. Superalloys consist of an FCC austenitic matrix called γ, plus a variety of secondary phases that may contribute to strengthen the alloy [12]. Secondary phases that contribute to control properties in all types of superalloy are the carbides MC, $M_{23}C_6$, M_6C, and M_7C_3 (rare). Principal strengthening phases by

chemical and coherency strain are the ordered FCC γ'-Ni$_3$(Al,Ti), found in iron-nickel and nickel-based superalloys, and the ordered bct (body-centered tetragonal) γ"-Ni$_3$Nb, found in alloys containing Nb or Ta. Undesirable phases may be observed due to variations in composition or processing or due to high-temperature exposure, like hexagonal η-Ni$_3$Ti, orthorhombic δ-Ni$_3$Nb, σ phase and Laves. The phase called σ is a hard and brittle phase with a tetragonal crystal structure and occurs in many binary and ternary alloys of transition elements [12, 24, 25]. Laves are nonequilibrium intermetallic compounds of the form AB$_2$, often with hexagonal closed packed crystal structure. The typical formula of Laves phase is (Fe,Cr,Mn,Si)$_2$(Mo,Ti,Nb), with many others intermetallic combinations observed in different materials [12, 26, 27].

Some alloying elements go into solid solution to provide oxidation resistance, phase stability and increased volume fractions of favorable secondary precipitates, and other elements are added to form hardening precipitates and/or intermetallic [12]. Cr is a major element in solid-solution hardening, while Co may be added up to 20% and Mo, W and Ta up to a total of 15%. These elements also dissolve in γ' so that the hardening effect may be twofold [24]. Many elements (Co, Mo, W, Re, Cr, etc.), under specific circumstances, may participate in the formation of undesirable phases like σ, μ, Laves, etc. [12].

Superalloys are commonly used in high-temperature service, and the properties of the grain boundaries in these conditions are as important as the strengthening by γ' within the grains. Grain boundary strengthening is produced mainly by precipitation of Cr and refractory metal carbides. These carbides have the morphology and stability enhanced by small additions of Zr and B [24].

Table 2.4 presents the alloying elements and their effects in superalloys.

Table 2.4: Role of different alloying elements in superalloys [12, 24].

Influence	Ni	Fe	Cr	Al	Ti	Co	Mo	W	B	Zr	C	Nb	Hf	Ta	Ce	La	Y	Re
γ' former	●			●	●													
MC former					●		●	●				●	●	●				
$M_{23}C_6$ former			●				●	●										
M_6C former							●	●				●						
M_7C_3 former			●															
Solid-solution strengtheners	●	●	●			●	●	●				●		●				●
FCC matrix stabilizers	●							●			●							
Hardening precipitates and/or intermetallic				●	●		●	●				●		●				
Grain boundary strengthening									●	●	●		●					
Oxidation resistance			●	●											●	●	●	

2.5.2 Nickel-based superalloys

In the last decades, nickel-based are the most used superalloys, and major applications are in turbine materials and jet engines, where they comprise 40–50% of the total weight of an aircraft engine [24, 7].

Nickel-based superalloys are strengthened by intermetallic-compound precipitation in an FCC matrix, from carbide precipitation or oxide-dispersion. For Ni-Ti/Al alloys the strengthening precipitate is γ'. Ni-Nb alloys, like IN718, the strengthening precipitate is γ''. Nickel-based superalloys may contain both Nb plus Ti and/or Al and be strengthened both by γ' and γ'' precipitates [12]. Figure 2.7 displays a typical two-phase γ-γ' microstructure of a single-crystal turbine-blade made in nickel-based superalloy, where is possible to observe γ' precipitates with a cuboidal morphology dispersed in the matrix.
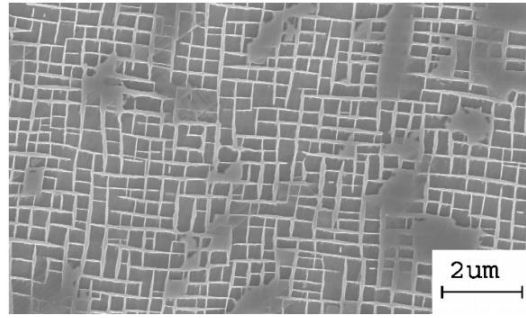
Figure 2.7: Microstructure of a nickel-based superalloy single crystal with a high-volume fraction of γ' precipitates [7].

After a long period in service, some nickel-based superalloys tend to form σ-phase that is brittle. The formation of the σ-phase happens when composition changes occur [24].

IN718 is a Ni-Cr-Fe superalloy with the addition of Nb to prevent cracking issues during welding. The superalloy IN78 is widely used in the aircraft engine industry due to its inherent corrosion resistance and excellent fabricability [28]. This alloy is known to be a precipitation hardening alloy, exhibiting this behavior mainly due to the precipitation of phases γ''(Ni3Nb) and γ'(Ni3(Al,Ti)) in the γ matrix after annealing over a long period of time in a temperature range of 620–720 °C [29].

On the other hand, segregation is a major concern in solidified IN718, with detrimental chemical inhomogeneities in the microstructure that affect the mechanical properties. Casting and weld metals present differences in their mode of solidification, thermal cycles experienced and the extent of segregation. Segregation of Nb- or Mo-containing phases is commonly observed in welded or deposited IN718 [29, 30].

The intermetallic laves phase, rich in Nb, forms in the interdendritic regions of as-deposited microstructure of IN718 and embrittles the material [31]. The formation of Laves phase causes detrimental effects in the matrix, depleting it of main alloying elements required for hardening, also forming a weak-zone microstructure between this secondary phase and the matrix and creates preferential sites for crack initiation and propagation because of its inherent brittle nature [30]. Laves are also known to promote the initiation and propagation of liquation cracking in the HAZ of welded IN718 [32]. Niobium is the element which promotes the formation of this phase in IN718 [25].

16

In addition, the morphology of the Laves greatly depends on the heat input and the cooling rate of the deposition process [30, 31]. It is expected that deposition processes with lower heat input and higher cooling rates produce lower fractions of the Laves phase [29]. Laves can be observed in the solidified microstructure of IN718 presented in Figure 2.8, where the precipitation of needlelike δ-phase is observed around the Laves particles in (a), along with some carbides, and dendritic fracture surface in (b).
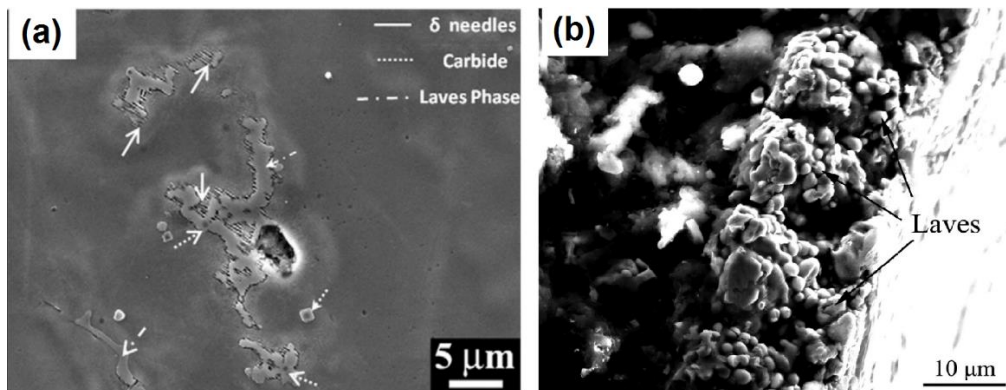
Figure 2.8: (a) Laves phase present in the microstructure of IN718 deposited with direct laser fabrication [33], (b) Laves present in the dendritic fracture surface typical of liquation cracking in laser additive manufactured IN718 [34].

2.6 Microstructure and properties aspects of repaired and microalloyed materials using ESD

Many studies have been conducted to comprehend the characteristics and performance of ESD deposited layers. Studies have been done to comprehend the morphology and distribution of defects, structure of deposited layer, precipitation of phases, distribution and segregation of material, effects on the base metal and properties related to modified surfaces or repaired pieces using ESD.

2.6.1 The presence of defects

In pieces repaired or coated using ESD the quality of deposition is a concern, since many porosities and defects may occur. Champagne *et al.* [35] used ESD to

repair AISI 9310 steel using IN718 as an electrode. They had been using respectively frequency, voltage and capacitance as 400 H$_Z$, 140 V, 30 µF. These parameters showed uniformity of the coating, clean interface between the coating and substrate, and diminished voids/cavities within the repaired cavity. Figure 2.9 shows the repaired cavity of AISI 9310 steel, with IN718 as filling metal, performed by Champagne *et al.* [35].
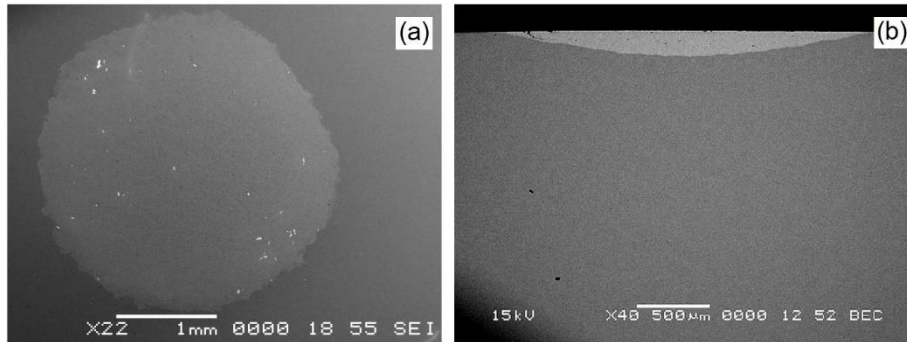
Figure 2.9: SEM image of the repaired cavity of AISI 9310 steel using Inconel 718 as filling metal: (a) top surface, (b) cross-section [35].

The presence of defects is an inherent feature of deposited materials when the ESD technique is used. An attempt to eliminate defects like porosities and cracks was performed by Radek and Bartkowiak, by applying Nd:YAG laser to remelt the ESD deposited layers of WC-Co-Al$_2$O$_3$ and WC-Cu [36, 37]. Figure 2.10 presents the microstructures of the alloyed layers before and after laser treatment. It is possible to observe a clear boundary between deposition and substrate in Figure 2.10(a), with many porosities and cracks within layers in the as deposited conditions, Figure 2.10(a) and (c). After Nd:YAG laser treatment, Figure 2.10(b) and (d), flaws like porosities and microcracks were diminished, giving to the microalloyed layer a more cohesive aspect.
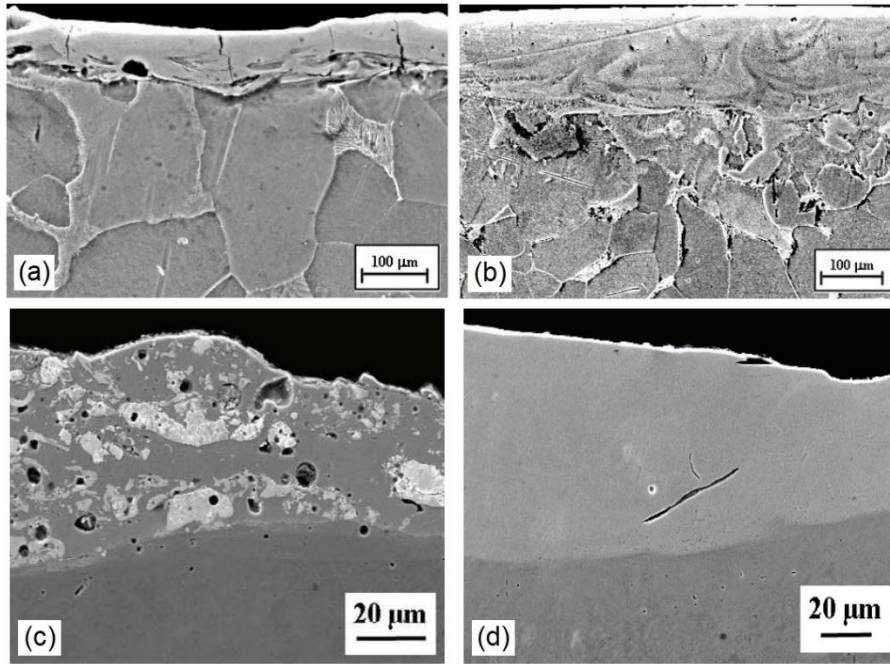
Figure 2.10: Microstructure of ESD alloying of: WC-Co-Al$_2$O$_3$ coating before laser treatment in (a) and after treatment in (b), WC-Cu coating before laser treatment in (c) and after treatment in (d) [36, 37].

2.6.2   The effects on the base metal

The little effect of ESD coatings on the base metal is one of the advantages of this technique, producing small or no Heat Affected Zone (HAZ) or precipitation of phases after the process [3]. Anisimov, Khan and Ojo [5], as well as Wei *et al.* [38] observed no effect on the base metal, like HAZ or precipitation of phases in their work using ESD to deposit respectively IN718 and Mo$_2$FeB$_2$. Ebrahimnia *et al.* [18] observed the presence of γ-γ'eutectic and MC carbides in the grain boundaries of the base metal in regions adjacent to the ESD zone and link the presence of such phases to the heavy elemental segregation in the as-cast base metal. Radek and Bartkowiak [36] detected little effect on the substrate, observing the presence of small HAZ in the interface deposition-base metal, as observed in Figure 2.10(a).

Jing and Tang [39] observed the formation of a small HAZ between the bonding zone and the substrate, as presented in Figure 2.11. Figure 2.11(a) shows a low magnification cross-section of the steel substrate coated with Co-Stellite 6, a cobalt-based superalloy, where no major cracks and porosities were observed. Figure 2.11(b)

shows a higher magnification image corresponding to the area "f" of (a), showing the interface coating/substrate where bonding zone and HAZ are depicted. The bonding zone corresponds to the area where electrode materials mix with the substrate materials. The formation of the HAZ is attributed to the repeatedly heating and cooling of the substrate surface during the ESD process.
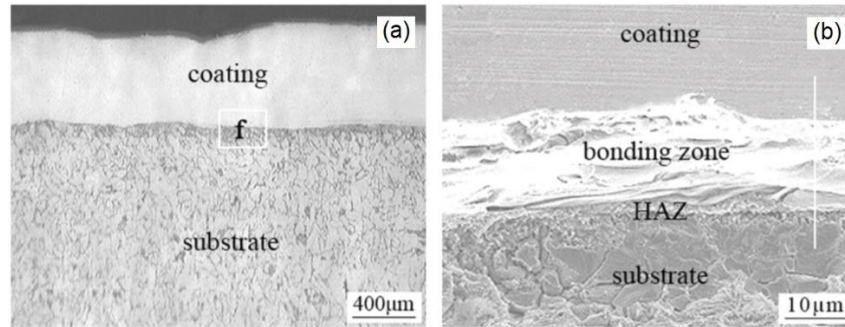
Figure 2.11: Cross-section showing the microstructure of carbon steel coated with cobalt-based Stellite 6: (a) low magnification, (b) high magnification of the area "f", showing the interface coating/substrate [39].

2.6.3 The microstructure of ESD deposited layers

Numerous authors have been studying the microstructure of ESD deposited materials. Anisimov, Khan and Ojo [5] studied the microstructure of ESD deposited Inconel® alloy 718. In this work, they observed that the grain size of the ESD layer is 4.7 ± 2.2 µm, with grains aligned along the ESD build-up direction. TEM analysis showed the presence of laves phase $(Ni,Fe,Cr)_2(Nb,Mo,Ti)$ and MC carbides (NbC, TiC) within deposited layers, as observed in Figure 2.12 (a). XPS analysis suggested the presence of oxides, and TEM revealed that oxides exist as nano-size (12–100 nm) particles, randomly dispersed in the ESD layers, as shown in Figure 2.12(b). The formation of the main hardening phase in this nickel-based superalloy, γ" precipitates, was not observed. The authors conclude that the presence of the oxides inhibited grain growth during heat treatment undertaken after deposition.
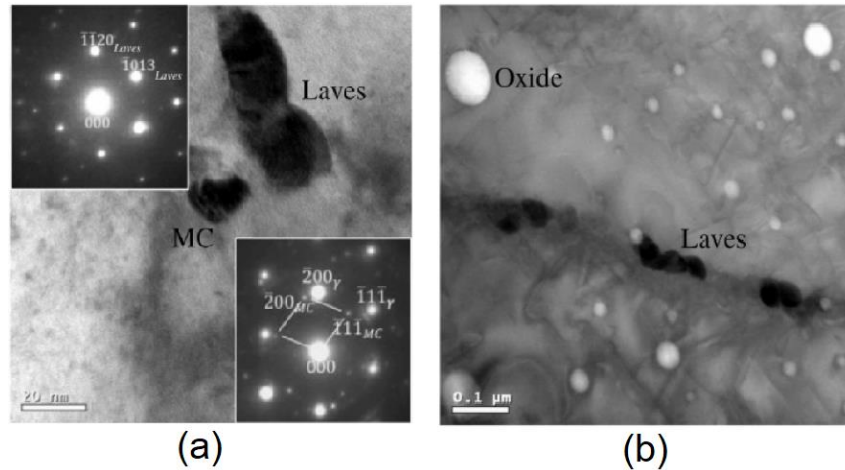
Figure 2.12: TEM images data showing the presence of Laves and MC carbides in (a) and spherical oxides in (b) within layers of ESD deposited IN718 [5].

The microstructure of the built-up layer of nickel-based superalloy IN738LC is discussed in the work of Ebrahimnia *et al.* [18]. The authors used the same material for electrode and base metal, with the base metal used in the as cast condition. The four-millimeter electrode was machined out from the base metal using electrical discharge machining (EDM)-wire cut machine. In this work, the authors used argon as shielding gas, with a flow rate of 15 L/min. The process parameters were electrode rotation speed of 2500 rpm, voltage 100 V, pulse frequency 250 H_Z. It has been shown that the deposited layer of IN738LC is formed by epitaxial growth on the base metal, with the same crystalline orientation. Discontinuities, like lack of fusion and porosities, act as nucleation sites, producing fine grains within the deposited layer, as depicted in Figure 2.13(a). EBSD analysis showed that very fine grains are observed in the deposited layer. The grains consist of fine grains of cellular γ phase, with precipitation of γ' within the grains, as shown in Figure 2.13(b). The precipitation of γ' occurred in the coating despite the extremely high cooling rates observed in the ESD process.
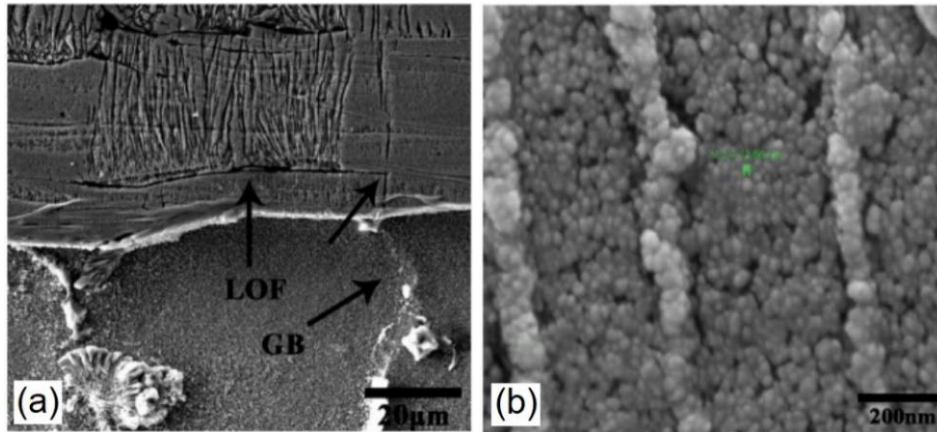
Figure 2.13: SEM images showing in (a) different discontinuities where new grains are nucleated, like lack of fusion (LOF) and base metal grain boundary (GB). In (b) the microstructure of cellular γ phase is revealed, with precipitation of γ' [18].

The microstructure of the high gamma prime superalloy IN792 deposited with ESD has been discussed by Xie and Wang [40] in their work. The microstructure of the deposited layers can be observed in Figure 2.14, with a region close to the base metal in (a) and a region close to the top surface in (b). Electrochemical etching using 10% oxalic acid under 6 V DC for three minutes was performed to reveal the microstructure of the deposited layer. The microstructure of the lower region, Figure 2.14(a), was considered finer that the microstructure of the upper region, Figure 2.14(b). Two forms of microstructure are observed in the deposited layer, the bond-like line and the grain boundaries. The bond-like line is parallel to the solid/liquid interface, which according to the authors is formed during the repetitive pulsed nature of the heat resource observed in the ESD process. Growing vertically, the columnar-like grains observed Figure 2.14(b) pass through layers along the build-up direction, with small and large columnar-like grains commonly seen. XRD spectrum showed that major phase observed in the deposited layer is γ-Ni, with γ (200) the strongest diffracted peak. The cellular structure of the solidified regions can be observed in Figure 2.14(c) and (d). The cellular structure is similar in both regions, where structures vertical to the build direction and parallel to the build direction, as presented in Figure 2.14(c) and (d), were observed. The average spacing of the cellular structure is about 0.8 μm. The presence of gamma prime phase was not detected in the deposition layer, indicating that the rapid solidification during the ESD process strongly suppressed precipitation of gamma prime phase.
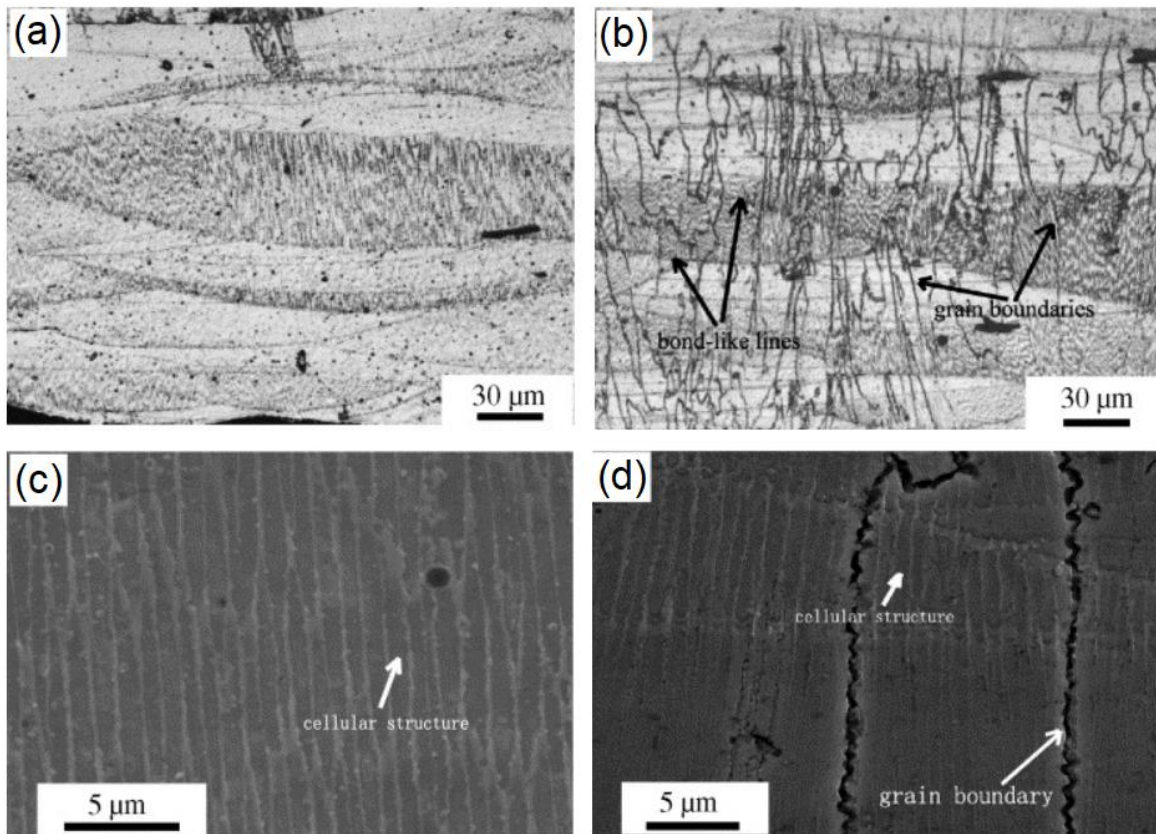
Figure 2.14: IN792 ESD deposited layer showing in (a) the microstructure of the lower region, (b) the microstructure of the upper region, (c) cellular structure of the lower region, (d) cellular structure of the upper region [40].

Phase contents and grain size of the ESD coating can be estimated using the Rietveld method, as accomplished by Wei *et al.* [38]. The authors applied Mo_2FeB_2-based cermet using ESD process on a high-speed steel substrate. It has been found that the mass fraction of amorphous phase and martensitic phase in the deposited layer are respectively 82% and 18%, with grain size of the martensitic phase of 31.7 nm in average. The authors suggest that the high cooling rate of the ESD process inhibited diffusion transformations, promoting the formation of amorphous and martensitic structures. The rapid cooling rate involved in ESD process may suppress elemental segregation and coarse carbides in weld metal [41].

2.6.4 The distribution of material

Some authors observed an uneven distribution of materials within deposited layers during the application of ESD. This inhomogeneous distribution of the elements

in the ESD coating was observed by Padgurskas *et al.* [4] and Wei *et al.* [38], as can be respectively seen in Figure 2.15(a) and (b). It is possible to observe in Figure 2.15(a) the unequal presence of Mo on the top surface of steel C45 coated with Mo, and in Figure 2.15(b) the different Mo content within deposited layer of high speed steel coated with Mo_2FeB_2. With this composition variation, the mechanical properties are expected to vary [4]. Mixed zones with macrosegregation of materials are expected when dissimilar materials are welded together autogenously. The macrosegregation is affected by convection or its absence [42].
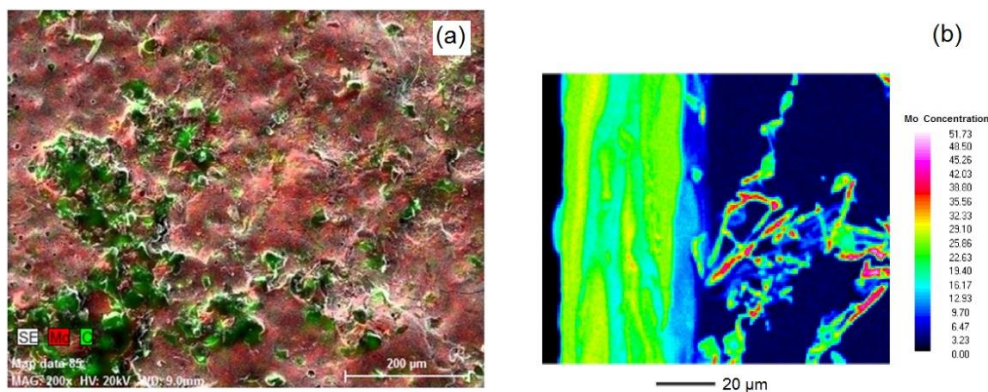
Figure 2.15: (a) Top surface of coating of C45 steel with Mo, showing composition distribution, (b) cross-section showing distribution of Mo after ESD coating of high-speed steel with Mo_2FeB_2 [4, 38].

On the other hand, Ebrahimnia *et al.* [18] observed very little elemental segregation in the ESD deposited layer of the nickel-based superalloy IN738LC, using the same material for electrode and base metal. Xie and Wang [1] state that a good homogenization of the coating is likely to occur due to the high cooling rates observed in the ESD process, suppressing microstructure coarsening and solute segregation.

2.6.5 Hardness of ESD deposited layers

The microhardness of ESD deposited layers has been studied by different authors. Padgurskas *et al.* [4] found that the hardness of coating in the Mo coated C45 steel increased for values of more than 1000 HV, while the hardness of the base metal is around 400. Durdu, Aktuğ, and Korkmaz [43] observed a considerable increase in hardness of the coated St35 steel with Ti_6Al_4V and attributed the increase in microhardness to the formation of hardened phases within layers. Jing and Tan [39]

24

found the average microhardness of the coating about 3.6 times of the substrate microhardness, arguing that the formation of strengthening phases during the ESD process, like the carbides Cr_7C_3 and Co_6W_6C, significantly improved the hardness of the coating. Anisimov, Khan and Ojo [5] believe that the strengthening of the ESD layer is highly influenced by nano-sized particles, like oxides, Laves phase particles and MC carbides, with minor contribution of the small grain size.

2.6.6 Roughness of ESD deposited layers

A characteristic feature of ESD deposited surfaces is high irregularity and roughness. Radek and Bartkowiak [36] analyzed the roughness of C45 steel coated with WC-Co-Al_2O_3, and a three-dimensional view of the surface after coating can be observed in Figure 2.16. The roughness average (R_a) of the coating was in the range from 6.16 to 7.79 µm, while the roughness of the steel specimens without coating varied from 0.39 to 0.41 µm. As can be seen in Figure 2.16, the maximum high of the peaks does not exceed 24 µm. Padgurskas *et al.* [4] observed the roughness of the ESD coated pieces in their tests, finding R_a and peak-to-valley height (R_z) of the alloyed surfaces varying respectively 2–3 µm and 8–10 µm before tribological tests, and respectively 0.3–2 µm and 2–9 µm after tests. Average R_a values for the Ti_6Al_4V coatings performed by Durdu, Aktuğ, and Korkmaz [43] was measured as 4.80 µm. Lešnjak and Tušek [44] observed that the roughness of the ESD deposited layers depends on the welding parameters, when higher welding parameter values lead to increased roughness.
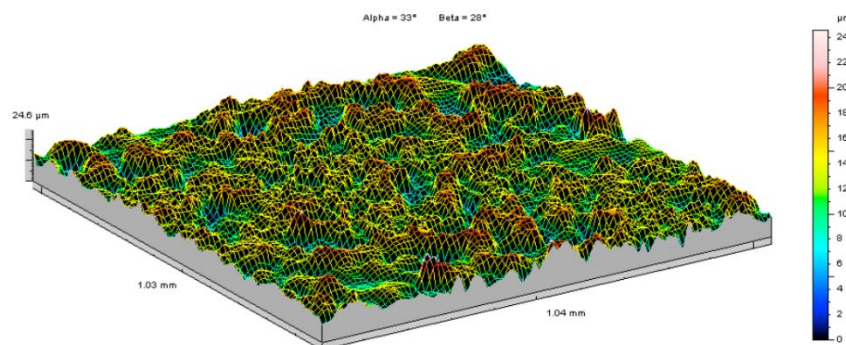
Figure 2.16: Topography of the surface of C45 steel coated with WC-Co-Al₂O₃ [36].

25

2.6.7 Wear and corrosion resistance of ESD coated materials

ESD coating has been applied to improve wear and corrosion resistance of elements subjected to extensive wear and/or working at corrosive environment.

Padgurskas *et al.* [4] coated C45 steel with different materials and compared the wear resistance under different loads. The authors observed and increased mass loss with increased load, but for molybdenum and chromiun coating. The molybdenum and chromium coatings showed low friction at loads of 1200 N during the tests, differently than the base metal. The friction coefficient practically presented no variance during the wear tests of molybdenum coated samples. Korkmaz [45] shows in his work that the friction coefficient of the coated St35 steel with Cr_7C_3 was lower than the base metal in sliding distances higher than 100 m, leading to a significant increase of wear resistance of steel coated by ESD process.

The corrosion resistance of substrates has been improved by ESD coatings. Liang *et al.* [46] ESD coated AISI 304, 310, and 430 stainless steel and Inconel 600 with pure aluminum and Ni20Cr alloy. Both Ni20Cr and aluminum coatings improved the corrosion resistance of the base metal. Korkmaz [45] determined the corrosion current density for coated St35 steel and uncoated steel, and found 3.6858 $\mu A \cdot cm^{-2}$ 4.7611 $\mu A \cdot cm^{-2}$ respectivelly. The coated steel presented lower corrosion current density, exhibiting a low corrosion rate with good corrosion resistance.

2.6.8 Performance of ESD repaired samples under tensile stresses

ESD repaired samples have been reported as strong as the base metal when exposed to tensile tests. Baghjari *et al.* [41] used 410 stainless steel as substrate, making two V shaped groves to be filled in with Alloy 82 using ESD. The microstructure of the repaired 410 stainless steel with Alloy 82 can be observed in Figure 2.17(a). The repaired grooves have a total thickness of more than one millimeter. Tensile tests were performed with test samples accordingly to the ASTM: E-8M for sub size sample. The results for tensile tests brought an ultimate strength around 425 MPa, rupturing the sample at the 410-base metal and not in the ESD repaired grooves, as observed

26

in Figure 2.17(b). The metallurgical bounding between the ESD layer and the base metal was considered strong.

Carofalo *et al.* [47] conducted tensile, fatigue and creep tests in flat Ni-based superalloy Waspaloy specimens repaired with ESD. They have found that samples repaired with ESD achieved better performance during tensile tests, with tensile strength close to the base metal. ESD and Micro Plasma repaired samples presented slightly reduced fatigue life when compared to the base material, in tests performed at room and 538 °C. It has been observed that after creep tests at the temperature of 704 °C, samples repaired with Micro Plasma presented creep behavior similar to the base metal, while ESD repaired samples presented a marked tertiary creep and higher strain rate. Carofalo *et al.* [47] were categorical, affirming that ESD technique is not suitable for repairing of components that may undergo high stresses.
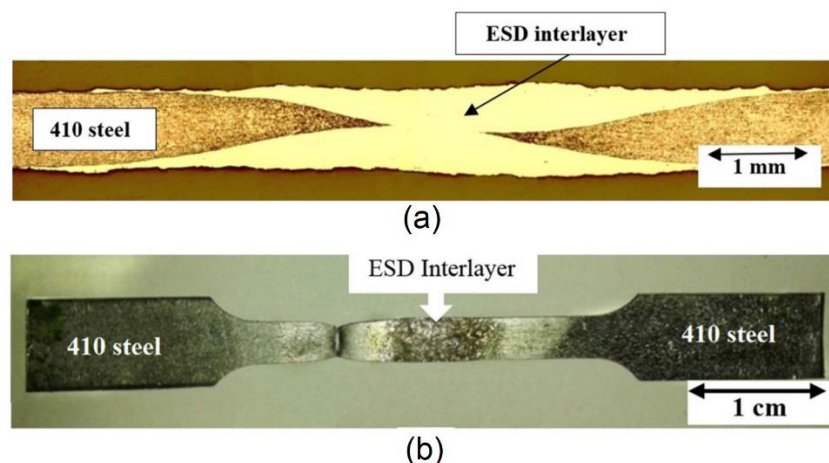
Figure 2.17: (a) cross-section showing the 410 stainless steel plate repaired with Alloy 82, (b) Tensile coupon of 410 stainless steel plate with ESD interlayer after test, with rupture in the base metal [41].

2.7   Material Transfer and Building-up Mechanism during ESD Process

2.7.1 Material transfer during the ESD process

As previously discussed, during the ESD process, the molten material from the tip of the rotating electrode is ejected onto the surface of the partially melted substrate.

The molten pool rapidly solidifies, forming the thin layer of coating. All the processes that occur during the ESD deposition are difficult to monitor due to the very short pulse duration and the small distance between the electrode and substrate [44]. Although the ESD brings a variety of advantages to repair or microalloy pieces, a mechanism that explains the actual process during the transfer of material, like the known modes of transfer for arc welding, is not well understood.

A material transfer mode similar to what is observed in gas metal arc welding (GMAW) is proposed by Johnson, *apud* Tang [19], being either globular or spray transfer modes. The globular mode of material transfer occurs in atmospheres containing air or nitrogen. The spray transfer mode happens in an atmosphere of ionized argon (Ar). An atmosphere containing Ar as shielding gas also produces a cleaning effect to the substrate surface, resulting in a smoother coating surface.

Johnson and Sheldon [3] state that the efficiency of material transfer from the anode (electrode) to the cathode (substrate) is influenced by the mode of transfer and the properties of the anode. Materials with lower melting points and lower heat capacities are believed to transfer more efficiently by the globular mode than by the spray transfer mode.

Lešnjak and Tušek [44] studied the material transfer during the ESD process using a high-speed camera and concluded that the material transfer through a conventional welding arc can be compared to the material transfer in the electrospark deposition process, with differences between these two processes being the manner in which the arc is burning. A conventional welding arc burns with practically no interruption, while the arc in the ESD deposition will ignite and extinguish irregularly. Accordingly to the observations, the material transfer is globular during the ESD process. The size and shape of the droplet is believed to depend on the welding parameters (current and voltage), the type of shielding gas, and the material of the electrode. According to the authors, the conventional short-circuiting material transfer observed in arc welding cannot occur because the ESD electrode is removed before arc ignition.

Galinov and Luban [48], propose that part of the molten material from the electrode is transferred through three distinct phases: vapor, solid and liquid. Vaporized portions of the electrode mostly dissipate in the environment, and particles

eroded in the solid form do not adhere to the electrode's surface, contributing to erosion material losses. Part of the material eroded in the liquid phase reaches the surface of the substrate will form the coating, and part rebounds from this surface, solidifying in the interelectrode gap. In addition, a small part of the liquid phase remains at the electrode surface.

2.7.2   Building-up Mechanism during ESD deposition

During the process of deposition using ESD, the thickness of the deposited layer may be limited due to the decreased dilution of the filer material by the substrate [44]. The subsequent layers are believed to diminish the dilution effect of the substrate [15]. The most important factor that controls the thickness of the deposited layer is the first contact of the electrode with the substrate. Moreover, the magnitude of the energy input in material deposition is important, and the higher the energy input, the thicker the deposited layer in the first material transfer [44].

Frangini and Masci [2] state that coating roughness create irregular contact surfaces that generate harmful transient arcs with high energy transfer and electrode overheating. Abundant surface melting of the electrode is considered by the authors as the most important factor in the production of irregular craters on the electrode surface and deposits with high roughness on the substrate.

As discussed before in the section 2.1, the solidified material in the form of splat or splash have a unique morphology as schematically presented in Figure 2.1(c), with solidified material building up on the sides of the splat. A similar morphology is proposed in Figure 2.18(a), which schematically shows a cross-section of a deposited splat (red). The substrate is depicted in blue. As the deposition continues with the electrode moving toward left, a second splat (green) is deposited over the previous splat as described in Figure 2.18(b). Three regions are observed in Figure 2.18(b). Region (1) is called to be the extremities of the splats. The region (2) is attributed to have high height due to the overlapping of splats, while the region (3) is believed to maintain the crater in the center due to splashing of material. Subsequent splats are expected to have a more uneven scattering of the material due to the increase of

roughness and peaks of the new substrate, like the area (2) depicted in Figure 2.18(b) suggests [49].
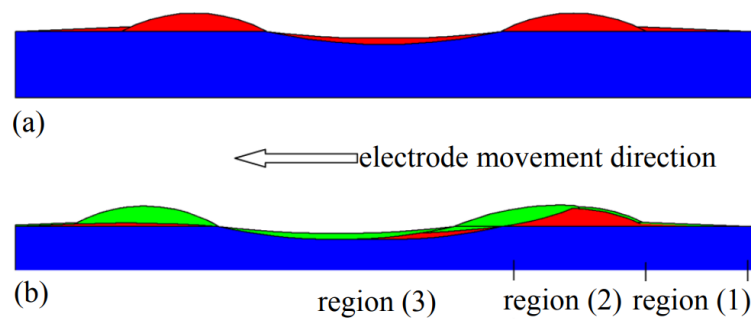
Figure 2.18: Representation of the material distribution of a single splat in (a) and the overlapping of a second splat (green) in (b) as the electrode moves from the right to left during deposition [49].

3. Chapter 3 – Materials and Methods

In this chapter, the procedures and equipment used to conduct this study will be presented. First, the materials used in this work will be detailed. Second, the equipment utilized for ESD deposition and repairing, data acquisition, metallographic preparation and etching, optical micrographs, elemental analysis and fractographies, surface analysis, microhardness and the equipment for tensile tests are presented. In the end of the chapter, the procedures to achieve representative deposition will be discussed.

3.1 Materials

For studies presented in Chapter 4 and Chapter 5 regarding the microstructure and microhardness of the depositions, the base metal consisted of a sheet of IN718, 1/8" thick, used in the as received condition, which is annealed without further treatments. Electrode used consisted of a rod of IN718, with diameter of 3 mm. For tensile studies presented in Chapter 5, bars of IN718 with diameter of 3/8" were received in the annealed condition.

The compositions of the sheet, rod and bars of IN718 are detailed in Table 3.1.

Table 3.1: Compositions of the materials used.

Element (%)	Ni	Cr	Fe	Nb	Mo	Ti	Al	Co	C	Mn	Si
Sheet	52.82	18.15	19.66	5.07	3.01	0.80	0.70	0.58	0.03	0.10	0.05
Rod	51.97	18.20	18.35	5.16	2.87	0.82	0.50	0.45	0.03	0.08	0.07
Bar	52.62	18.38	18.69	5.12	2.92	0.90	0.54	0.38	0.03	0.08	0.06

Samples for tensile tests were mechanically machined and are presented in the final dimensions in Figure 3.1(a) for base metal and previously to the repairing in Figure 3.1(b) and Figure 3.1(c). After repairing, the samples were machined in a lathe to have a smooth finishing of the repaired region.
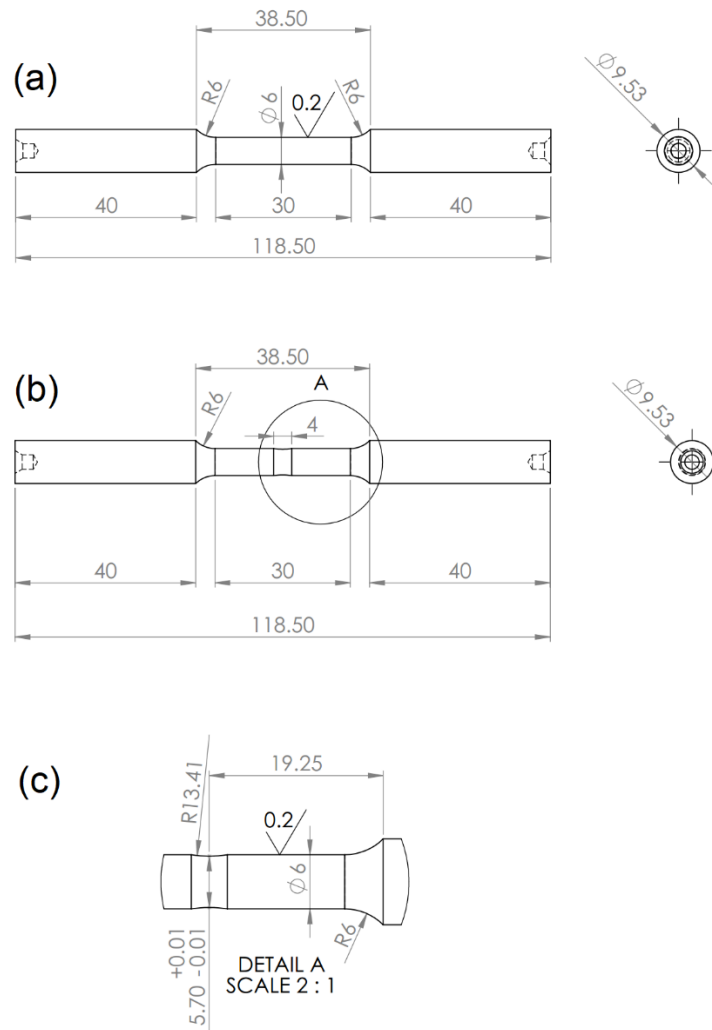
Figure 3.1: (a) dimensions of the tensile samples for the base metal. (b) dimensions for the notched samples and repaired samples before repairing. (c) detail of the groove and reduced section. Dimensions in mm.

3.2   Equipment

3.2.1 Equipment for ESD deposition

The ESD machine used in this study is the model M6300, with applicator model PD002 provided by Huys Industries Ltd. The machine and the applicator are shown respectively in Figure 3.2(a) and (b). The ESD machine has a control panel where it is possible to set the electrical parameters used in this study, such as the ESD voltage, the capacitance and pulse frequency. The ground is attached to the piece to be coated by clamping. The PD002 applicator connects to the shielding gas outlet and applicator attachment on the front panel of the ESD machine. The shielding gas used in this

thesis was is ultra-pure Argon, that is conducted through the machine and is will applied to the weld pool through a nozzle that converge the flux of gas to the area of interest.
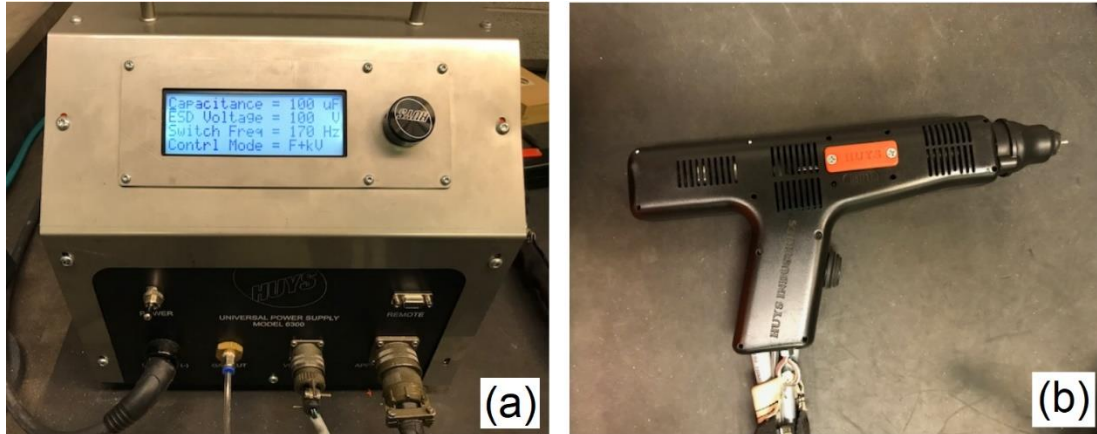
Figure 3.2: (a) ESD machine model M6300. (b) applicator model PD002.

3.2.2 Data acquisition

In order to acquire current and voltage during the ESD process, a NI-DAQ USB 6003 data acquisition system was used, in connection to a laptop via USB door and operating using the NI LabVIEW software. Voltage was measured stepping down the voltage and connecting the ESD power supply to an analogue input from the NI-DAQ device. Current was acquired via the Hall Effect sensor of the machine integrated with the NI-DAQ system.

3.2.3 Metallographic preparation and etching

The samples were prepared for microstructural analysis following standard metallurgical preparation, first sectioning the samples in the middle of the depositions using a precision saw Accuton-50. Subsequently, the samples were hot mounted using conductive bakelite (Struers Polyfast^{Tm}), then ground and polished using diamond spray. Etching for optical microscopy were done using inverted glyceridea and electrochemical etching with oxalic acid 10% as reagent. The software ImageJ was used to perform image analysis including deposition thickness measurements, and defects distribution analysis.

3.2.4 Optical micrographs, elemental analysis and fractographies

Optical microscopy was performed using an Olympus BX51M System metallurgical microscope with integrated digital camera for capture of images.

For observation of microstructure and fractographies, the Scanning Electron Microscope (SEM) Zeiss UltraPlus Field Emission SEM has been used. The same microscope with an energy dispersive spectroscopy (EDS) microanalysis system was used for elemental analysis and mapping of elements.

3.2.5 Surface analysis

Surface analysis for determination of the roughness and peak-to-valley distance of the ESD depositions was performed using WYKO NT1100 optical profiler in the VSI mode. The data obtained through the optical profiler was examined using the Wyko Vision® analysis software which is directly linked to the optical profiler. Figure 3.3 shows an image of the optical profiler.

Figure 3.3: WYKO NT1100 optical profiler.

3.2.6 Microhardness

Microhardness tests were performed using a Wilson Vickers 402MVD automated hardness tester, with 10 g load and dwell time of 15 s. All the microhardness tests were carried out following the procedures of the standard ASTM E384-16. The samples were prepared accordingly to the usual metallographic preparation of grinding and polishing followed by etching with inverted glyceridea. Figure 3.4 shows a picture of the microhardness tester.

Figure 3.4: Microhardness tester.

3.2.7 Tensile tests

Tensile samples were painted using two layers of paints, the first being a base of white paint and the second a black paint that created the dot appearance on the surface of the samples. This kind of painting was applied to create the black dots that would work as references during the tensile tests using the Digital Image Correlation (DIC) technique. Figure 3.5 shows tensile samples after the application of the two layers of painting. Masking tape was applied to the extremities of the samples to avoid uneven and slippery surfaces on the gripping areas of the samples.

Figure 3.5: Tensile samples after the application of the two layers of painting.

The tensile tests were conducted using the DIC technique in an MTS 810 frame with 50 kN of capacity. Two cameras of 5 megapixels were used to capture the images during the test. The setup of the machine with the cameras positioned in front of the frame is shown in Figure 3.6. The software Aramis V.6.3.1-1 for acquisition of images and posterior analysis was used synchronized with the MTS frame and cameras during the tensile tests. The displacement rate during the tensile tests was kept constant in 0.6 mm/mim, in accordance with the standard ASTM E8/E8M – 16.

Figure 3.6: Setup of the MTS frame with the cameras for tensile tests using the DIC technique.

3.3   Methods

Initially, nine conditions called Condition 1 to 9 (C1 to C9) were proposed to be studied in this research work. The conditions were selected based on previous studies and tests that showed that with capacitance and voltage higher than 120 µF and 120 V, the quality of the deposition is deteriorated. A matrix showing the electrical parameters for the initial conditions is described by Figure 3.7. The capacitance (C) and voltage (V) were the variables, while the frequency was kept constant at 170 Hz during the studies. To better characterize the effect of capacitance and voltage on the ESD deposited IN718, a row and a column with constant capacitance and voltage, and variable voltage and capacitance were selected. The row with constant capacitance of 120 µF and variable voltage was selected, corresponding to conditions C1, C2, and C3, along with the column where the voltage of 100 V is constant, and the capacitance is variable, corresponding to conditions C2, C5 and C8. C10 was posteriorly added to the matrix of experiments to gain productivity during the repairing of groves using the ESD process.
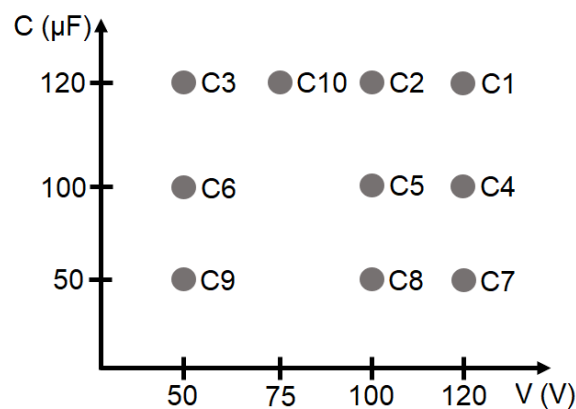
Figure 3.7: Matrix of experiment showing the electrical parameters used to study the ESD repaired IN718 from Condition 1 (C1) to Condition 10 (C10). The pulse frequency used was 170 Hz.

In order to evaluate the effect of frequency on the defects and roughness of ESD deposited IN718, five more conditions were evaluated. The conditions comprise of Condition 1 (C1) and Condition 2 (C2) with additional pulse frequencies that are different to that used on the conditions presented in Figure 3.7. The new frequencies used for C1 are 85 Hz and 64 Hz, and the new frequencies used for C2 are 300 Hz, 85 Hz and 64 Hz.

ESD deposition was carried out by passing the ESD applicator in a raster pattern ensuring overlapping between each of the deposited line. The above was repeated twice for each specimen investigated with the raster pattern of the first pass from left to right, whereas the raster pattern of the second pass was from back to the front.

4. Chapter 4 – Defects formation during electrospark deposition of Inconel 718

In this chapter, mechanisms are proposed and discussed to explain the formation of defects during ESD depositions made with different pulse energies and pulse frequency.

4.1 The formation of defects in electrospark deposited IN718 with six different pulse energies

The pulse energy correlated to the six conditions studied has been calculated using the Equation 1, and the values of pulse energy for each condition are presented in Table 4.1, as well as the used electrical parameters. The overall pulse energy of the ESD process was varied by varying the voltage and capacitance and keeping the frequency (170 Hz) constant for all experiments discussed in this section.

Table 4.1: Pulse energy for six conditions studied.

	C1	C2	C3	C5	C8	C10
Condition	120 V 120 µF	100 V 120 µF	50 V 120 µF	100 V 100 µF	100 V 50 µF	75 V 120 µF
Pulse energy (J)	0.864	0.600	0.150	0.500	0.250	0.338

Figure 4.1 shows representative optical micrographs of the deposited layers for the six conditions studied. The edges of the deposited layer have been indicated by the white dashed lines in Figure 4.1. The thicknesses of the deposited layer for pulse energy of 0.864 J (C1), 0.600 J (C2), 0.150 J (C3), 0.500 J (C5), 0.250 J (C8) and 0.338 J (C10), were measured to be respectively: 343 ± 138 µm, 264 ± 45 µm, 63 ± 9 µm, 303 ± 116 µm, 149 ± 23 µm, and 86 ± 17 µm. The tolerances are the standard deviation of the mean. It is observed that the thickness of the deposited layer is increased with the intensification of the pulse energy. The increase in thickness is expected, since more material is transferred during the process with higher energy [1, 50]. Although C10 has a higher pulse energy than C8, it seems that the voltage plays a leading role in the material transfer, since C8 has higher voltage and a thicker deposited layer.
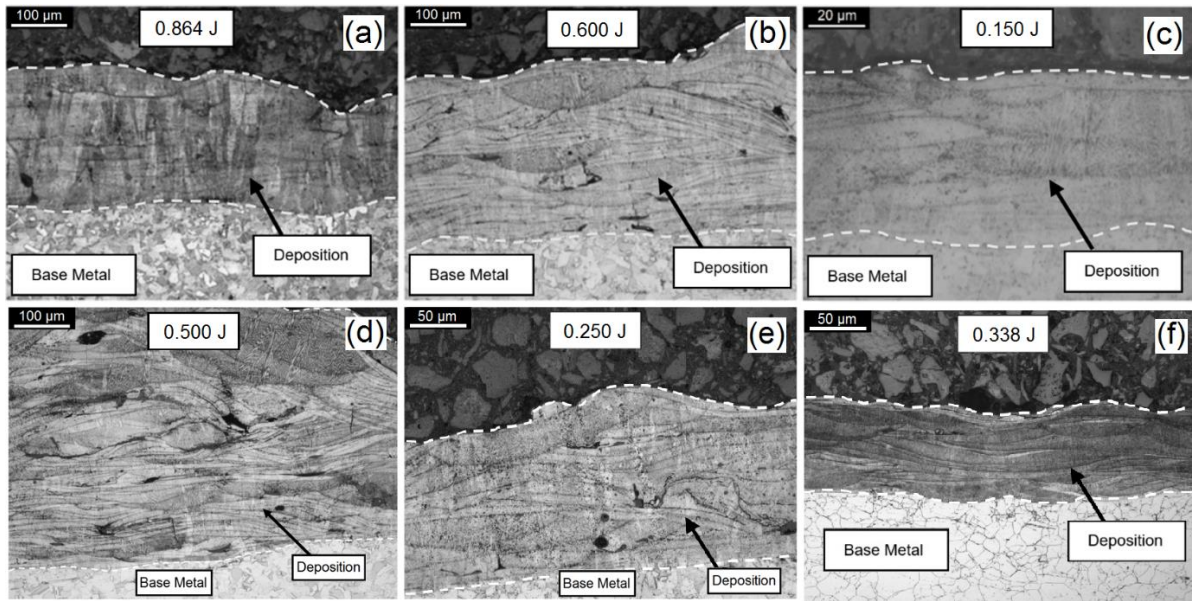
Figure 4.1: Deposited layers for six pulse energy studied. High pulse energy produced a thicker and more uneven deposited layer. Different scales are observed. Inverted glyceridea etchant

Defects like insufficient fusion, voids and cracks are commonly observed in depositions made with ESD [4, 50, 51]. A map showing the morphology and distribution of defects within the deposited layers can be observed in Figure 4.2. The images in Figure 4.2, which respectively correspond to the area of each deposition presented in Figure 4.1, were obtained using the threshold function of the software ImageJ. As can be observed in Figure 4.2, the morphology of defects is different for the three depositions. Defects like cracks and insufficient fusion are abundant in deposition with high pulse energy, as observed in Figure 4.3. Areas where insufficient fusion occurred can be attributed to the rapidly solidification of splats in the ESD process, resulting in areas were the splats solidified creating misruns areas, with incomplete cavity filling. On the extremities of the splats the solidification is rapid due to the thinner material distribution leading to increased heat absorption by the substrate and previous splat.

Areas with insufficient fusion are also observed in the deposition with intermediate pulse energy, like C2 and C5. Lack of boundary (LB) is commonly observed in ESD deposited layers and appear as elongated cracks perpendicular to the build-up direction. For pulse energy of 0.150 J (C3) and 0.338 J (C10), defects like

LB and microvoids are also observed, but massive voids where insufficient fusion occurred are not detected in those depositions.
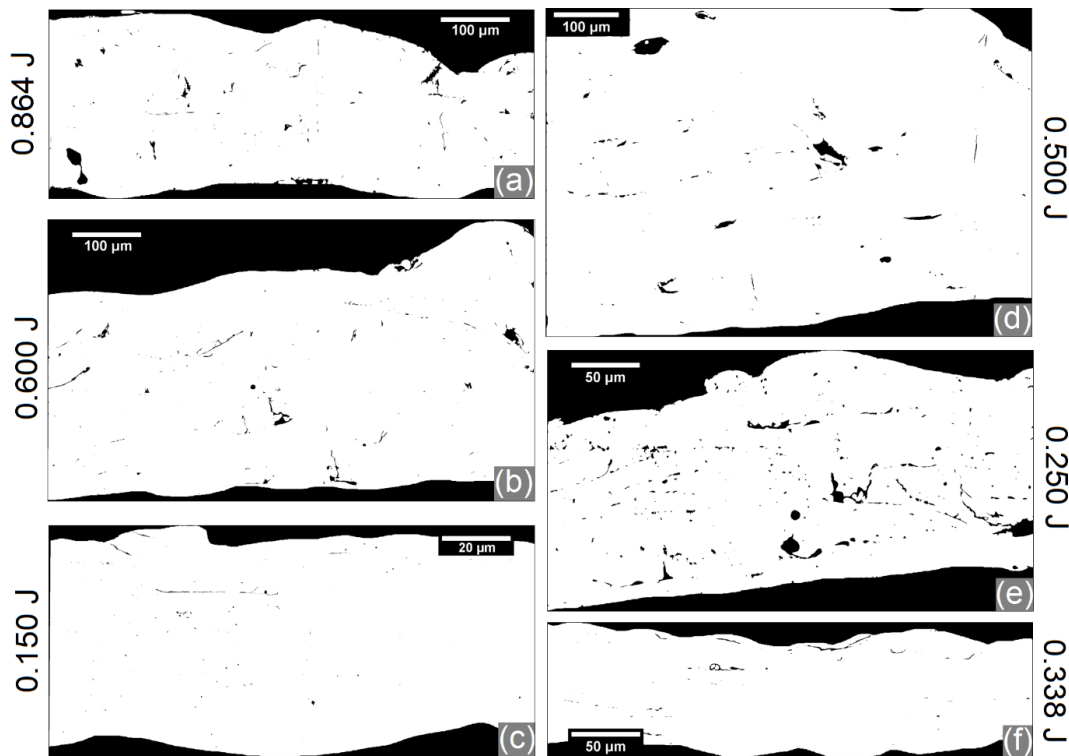
Figure 4.2: Map of defects showing morphology and position of flaws within each deposited layer. The morphology and distribution of defects is different for different pulse energy. Different scales are observed.

Cracks, like those observed in Figure 4.3, are also observed in depositions made with intermediate pulse energy (C2 and C5), and are attributed to the differing extent of thermal contraction of the material caused by large temperature gradients and rapid solidification during the ESD process [4, 38].
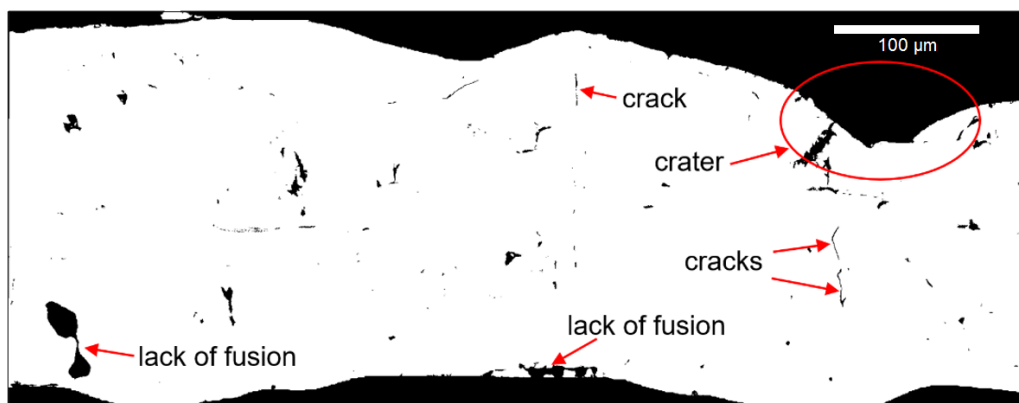
Figure 4.3: Map showing details of defects. Pulse energy of 0.854 J (C1).

The SEM image of Figure 4.4(b) shows the point of nucleation of one of the cracks observed in the deposition made with highest pulse energy. It is possible to observe that the crack initiated in a defect like LB, where a point of stress concentration occurs, acting as a susceptible site for nucleation of cracks. The combination of thermal contraction and stress concentration contributed to the nucleation of cracks on the microstructure of higher pulse energy depositions. Craters, observed in Figure 4.3, are commonly detected in depositions with high voltage and capacitance, contributing to the formation of cold laps as observed on the right of the crater in Figure 4.3 and Figure 4.4(a). In thin solidification sections, like those areas in the extremities of ESD splats, heat loss from the liquid metal during the spread of the material may result in premature freezing, producing surface defects like cold laps or misruns [52].
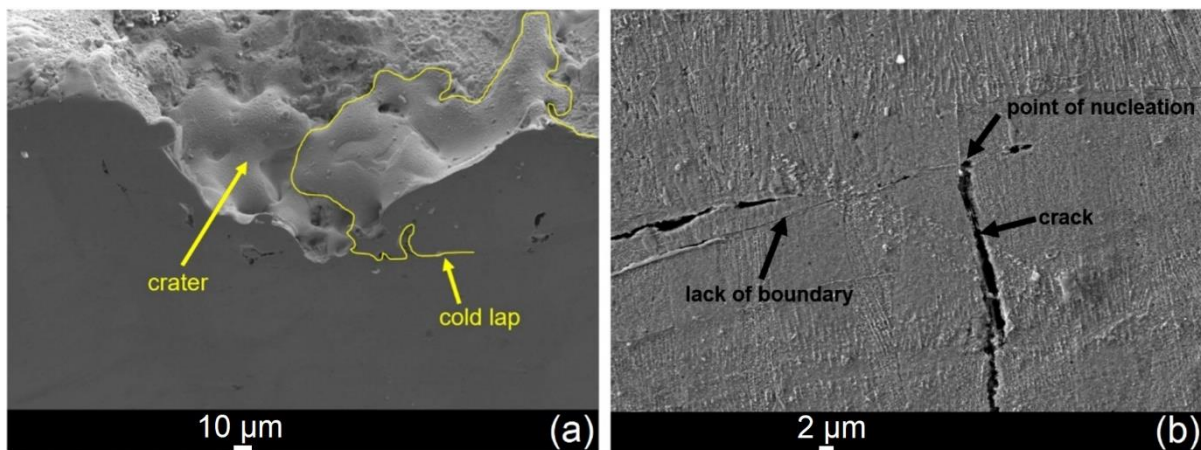
Figure 4.4: (a) Tilted view showing a cold lap on the edge of deposition, (b) point of nucleation of a crack. Pulse energy of 0.854 J (C1). Inverted glyceridea etchant.

Indeed, the precipitation of intermetallic phases can utterly degrade the ductility of high-strength high-temperature alloys, like the IN718 [12]. Intermetallic phases produce sufficient local stress concentration to nucleate and propagate cracks because of its inherent brittle nature [53, 54]. Areas where cracks appear in the deposited layer of IN718 using C2 can be observed in Figure 4.5(a). Figure 4.5(a) also depicts the presence of intermetallic segregation and defects commonly observed in that deposition.
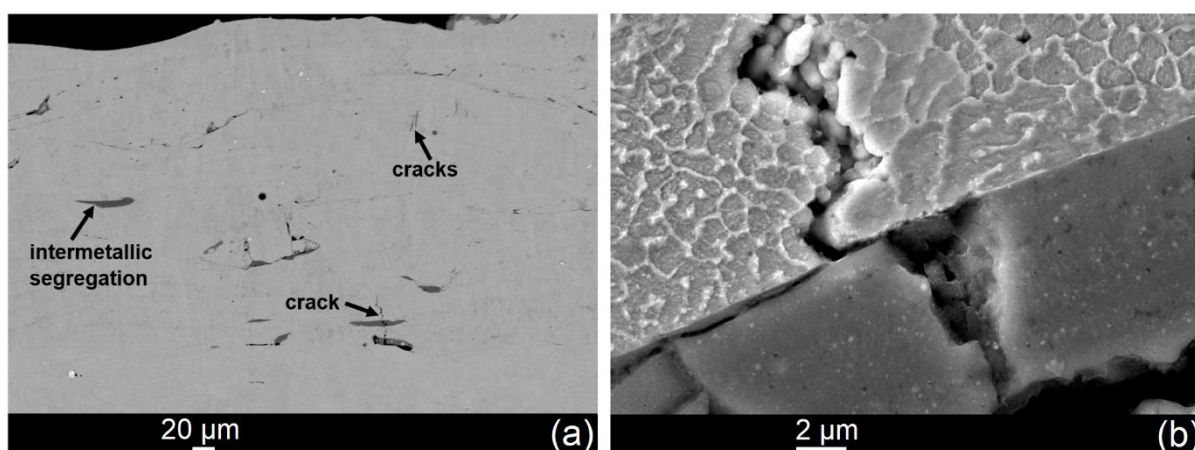
Figure 4.5: (a) SEM image using backscattered diffraction showing deposition made with C2 with cracks and intermetallic segregation within the deposited layer. A close view showing a crack that propagate through the interface of an intermetallic particle and the base metal in a deposition made with C1.

In fact, the presence of intermetallic segregations in the ESD deposited layers of IN718 appears to contribute to the formation and propagation of cracks during the solidification of the fusion zone. It is observed that the coarse intermetallic particles may contribute to the propagation of cracks, like observed in Figure 4.5(a) and (b). Those cracks observed in depositions with high pulse energy, that propagated in the vicinity of intermetallic segregation, were not observed in the ESD deposited layer made with pulse energy lower than 0.400 J. A detailed discussion about the features of the intermetallic segregation on the ESD deposited layer of IN718 is presented on the section 5.1.

The average area of defects (considering area of intermetallic as deposition) for each deposition, with measurements made in three different areas of each specimen, can be observed in Table 4.2 and Figure 4.6.

Table 4.2: Average area of defects for the conditions studied.

	C1	C2	C3	C5	C8	C10
Pulse energy (J)	0.854	0.600	0.150	0.500	0.250	0.338
Area of defects (%)	1.71 ± 1.00	1.34 ± 0.45	0.27 ± 0.15	1.43 ± 0.39	0.50 ± 0.16	0.37 ± 0.16

The area fraction of defects increases with intensified pulse energy. With the increased set voltage and consequent pulse energy, the current increases during the discharge of the capacitors in the ESD process, as discussed in section 4.3, and the effect of the resistive heating on the tip of the electrode is expected to rise with increased peak current. The exact mechanism of material transfer is not in consensus among scientists that study the mechanisms of material transfer during the ESD process. The small gap between electrode and substrate, combined with very small and short spark make difficult to observe the mechanism of material transfer [48]. In the ESD process, the emission of small molten droplets during the spark breakdown and subsequent attachment to the substrate may occur through different modes, like spray or streamer transfer [2, 48]. With high pulse energy, more electrode material is being melted, and considerably scattering of material is expected to occur during the material transfer. It is important to note that the electrode is constantly in contact with the substrate, and a short-circuiting transfer mode may occur, with violent reignition of the arc during the rotation of the electrode, resulting in considerable scattering of material. With the scattering of material during the material transfer, a strongly irregular distribution of molten material is expected, with formation of voids and laps like those observed in Figure 4.3 and Figure 4.4(a).
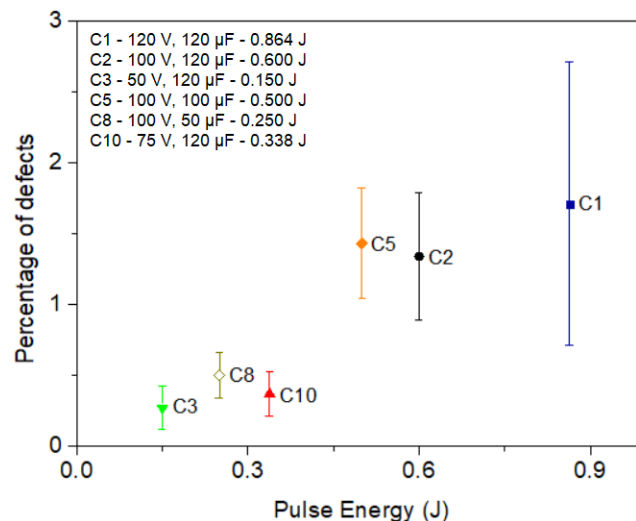
Figure 4.6: Area of defects for six conditions studied.

Figure 4.7 shows the curves for cumulative frequency of defects for the six conditions. It is observed in Figure 4.7(a) that more than 95% of the area of defects for the lowest pulse energy (C3) correspond to defects less than 5 μm^2 in area. C10 presents a similar trend to C3 for defects bigger than 7 μm^2. C8 has defects with bigger

44

size than the defects observed in C10, although the former condition has a lower pulse energy and average peak current. It is observed in Figure 4.7(a) and (b) that the conditions C1, C2 and C5 presented an analogous tendency for the size of the defects greater than 10 μm^2 observed within the deposited layer, regardless the differences in pulse energy and peak current.
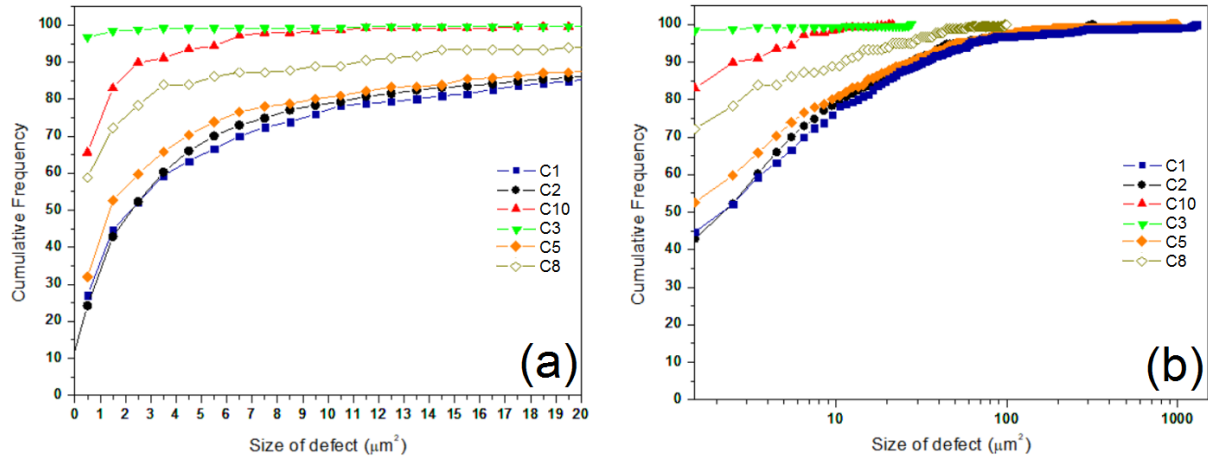
Figure 4.7: Cumulative frequency for six conditions studied.

4.2   Surface roughness as function of the pulse energy

The as-deposited surface of the six conditions can be observed in Figure 4.8. As the voltage is increased, as well as pulse energy, the topography of the surface is changed, showing a rougher surface with more craters and irregularities. The surface roughness (R_a) of ESD coated materials is commonly reported to increase with increasing mass transfer and pulse energy [1, 55].

C1 - 0.854 J	C2 - 0.600 J	C3 - 0.150 J
200 μm (a)	200 μm (b)	200 μm (c)
200 μm (d)	200 μm (e)	200 μm (f)
C5 - 0.500 J	C8 - 0.250 J	C10 - 0.338 J
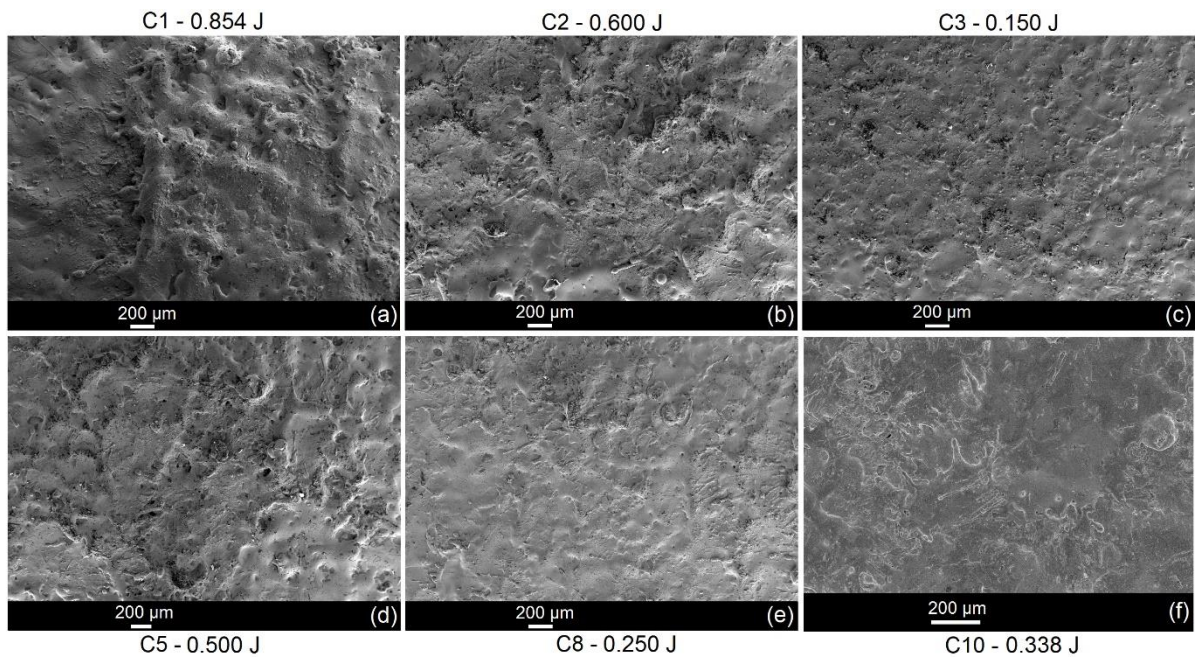
Figure 4.8: Top surface of the depositions.

Figure 4.9 presents the topography of the samples after ESD deposition. Peaks with height more than 60 μm are commonly observed in depositions with higher pulse energy, as shown in Figure 4.9(a), while lower peaks are observed in Figure 4.9(c) for the lowest pulse energy observed (C3), where most of them are less than 30 μm high. Deep craters and high peaks are observed in deposition with higher pulse energy, Figure 4.9(a), (b) and (d), while shallower cavities and lower peaks are observed in Figure 4.9(c) and (f) for lower pulse energy deposition. The statistics referring to the roughness of each surface are given in Table 4.3. It is observed a decrease in roughness as the voltage decreases. The R_a presents a major decrease for lowest pulse energy, closer to the average roughness of the base metal in the condition as received, which is 1.85 μm. The difference between the R_a of C1 and C3 practically doubles.
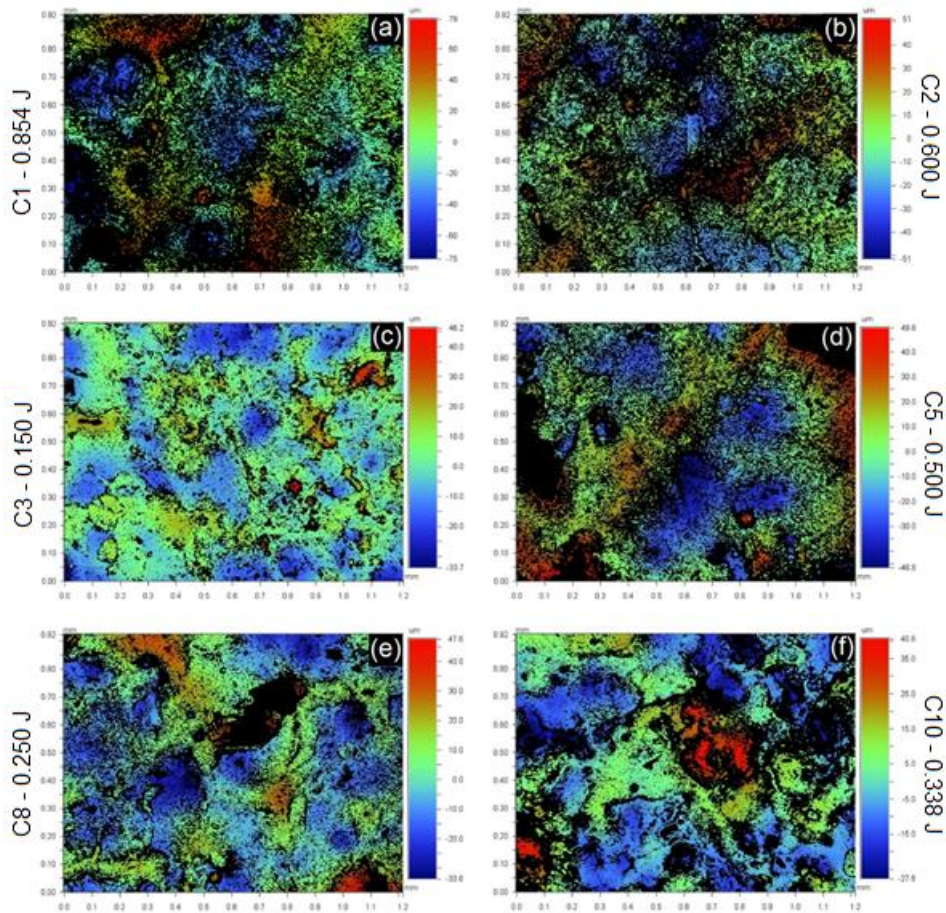
Figure 4.9: Topography of the surfaces for six conditions studied. Note the difference in scale within the color map. Dark areas are regions that exceed the range of measurement of the equipment.

The peak-to-valley height (R_z) indicates the maximum absolute value from top of the highest peak to the bottom of the deepest valley in that profile. It is observed that R_z of the deposition with highest pulse energy (C1) is higher than the value for the deposition with lowest pulse energy (C3) by approximately 55%, indicating an extensive formation of craters in deposition with higher pulse energy than in lower energy.

The surface texture and roughness of the layer may affect the formation of defects, since ESD is not a process that melts a large portion of the substrate and the distribution of material during the formation of splats is not uniform [19]. The spark discharge in the ESD process forms through the shortest interelectrode gap [55]. High peaks like those observed in depositions with high pulse energy will contact first the tip of the electrode, being the point for discharge of current. The subsequent material transfer will be uneven, as expected in ESD process, and the molten material may not

reach the bottom of deep cavities or craters, like the crater observed in Figure 4.4(a) or deep cavities like those observed in Figure 4.9(a), (b) and (d). In this case, the molten material detached from the electrode begin to build-up on the side of the craters, contributing to the formation of defects like insufficient fusion and cold laps, as represented by Figure 4.4(a).

Table 4.3: Surface statistics for the conditions studied. The values are an average of three measurements over the deposited layers.

	C1	C2	C3	C5	C8	C10
Surface statistics	0.854 J	0.600 J	0.150 J	0.500 J	0.250 J	0.338 J
R_a (µm)	16.11 ± 2.50	13.57 ± 2.61	8.06 ± 1.79	15.11 ± 1.76	10.52 ± 0.75	9.34 ± 1.42
R_z (µm)	112.66 ± 26.96	96.33 ± 7.51	72.80 ± 6.62	96.89 ± 4.09	83.86 ± 6.29	71.94 ± 4.57

4.3   The effect of pulse frequency on the quality of ESD deposited IN718

In this section, the effect of pulse frequency on the quality of the ESD deposited IN718 is discussed. The term total energy has been introduced in this discussion to refer to the energy observed in intervals of 0.1 second for each condition to differ from the pulse energy approach, since through this approach previous comparisons have been done between deposition made with pulse frequency of 170 Hz.

4.3.1 Current and total energy of depositions made with 170 Hz

Figure 4.10 presents the profile of pulses when a maximum spark current is observed during the ESD process. The peak current occurs when the capacitors are partially discharged.

Pulses of current are observed for the referred conditions in an interval of 0.1 second in Figure 4.11. There are seventeen pulses of current in that period. The total energy within this period was obtained by integrating the power over the time for each condition studied. The pulses of current were taken in three different periods of 0.1 seconds during the ESD process for each condition, and the average of total energy can be seen in Table 4.4.

48
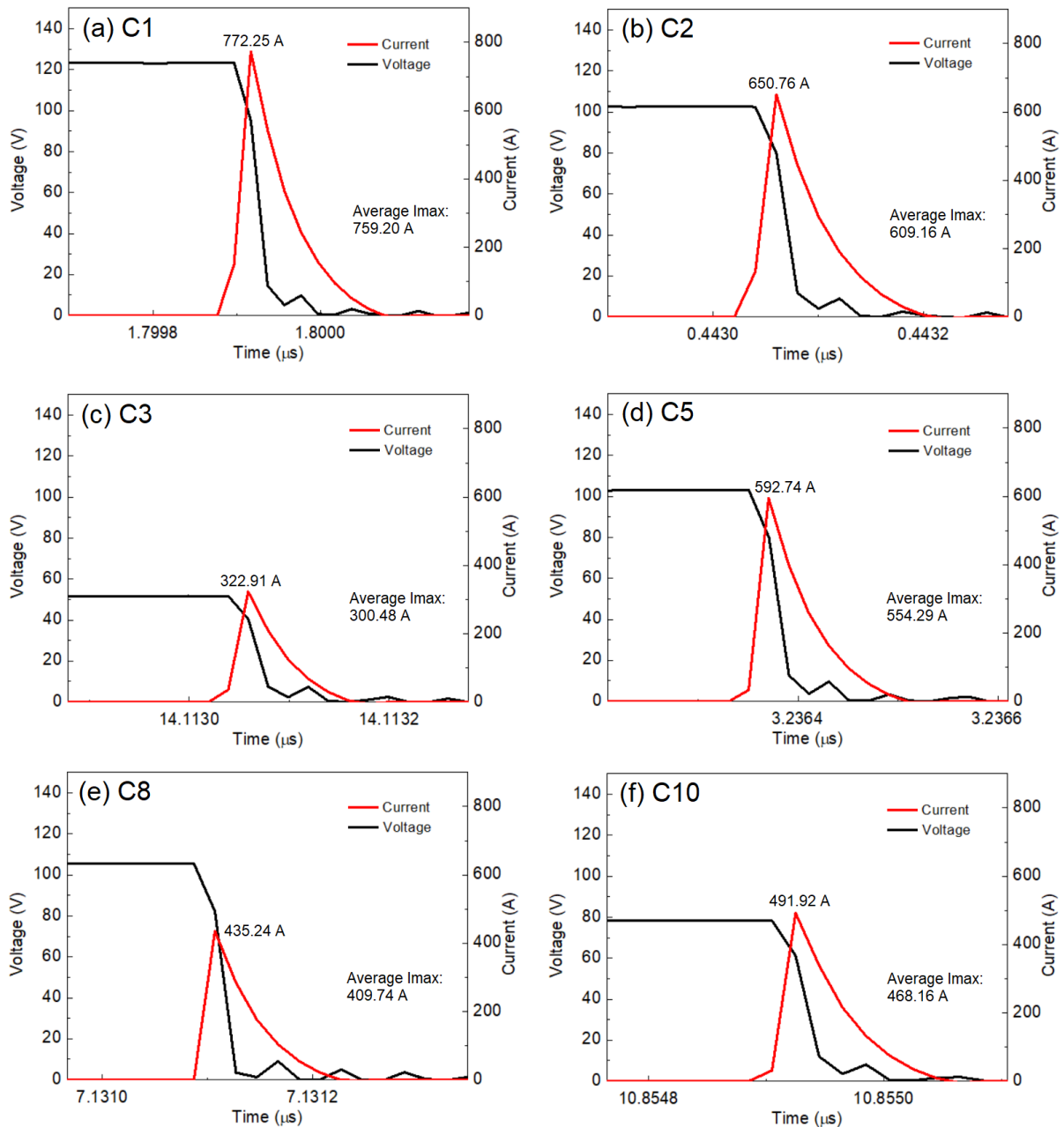
Figure 4.10: Voltage, maximum peak current and average maximum current during the ESD discharge for different conditions studied. The peak of current occurs when the capacitor is partially discharged. The average maximum current (I_{max}) is an average of the 200 highest peak current observed during the process.

Although C8 has practically the same total energy as C10, the average area of defects of C8 is slightly higher than C10, as observed in Table 4.2 and Figure 4.6. This inconsistency may be explained due to the nature of the ESD process, that inherently has a vast range of variables that may affect the formation of defects in depositions made with close pulse energy and average maximum current, which is the case of C8 and C10.

49
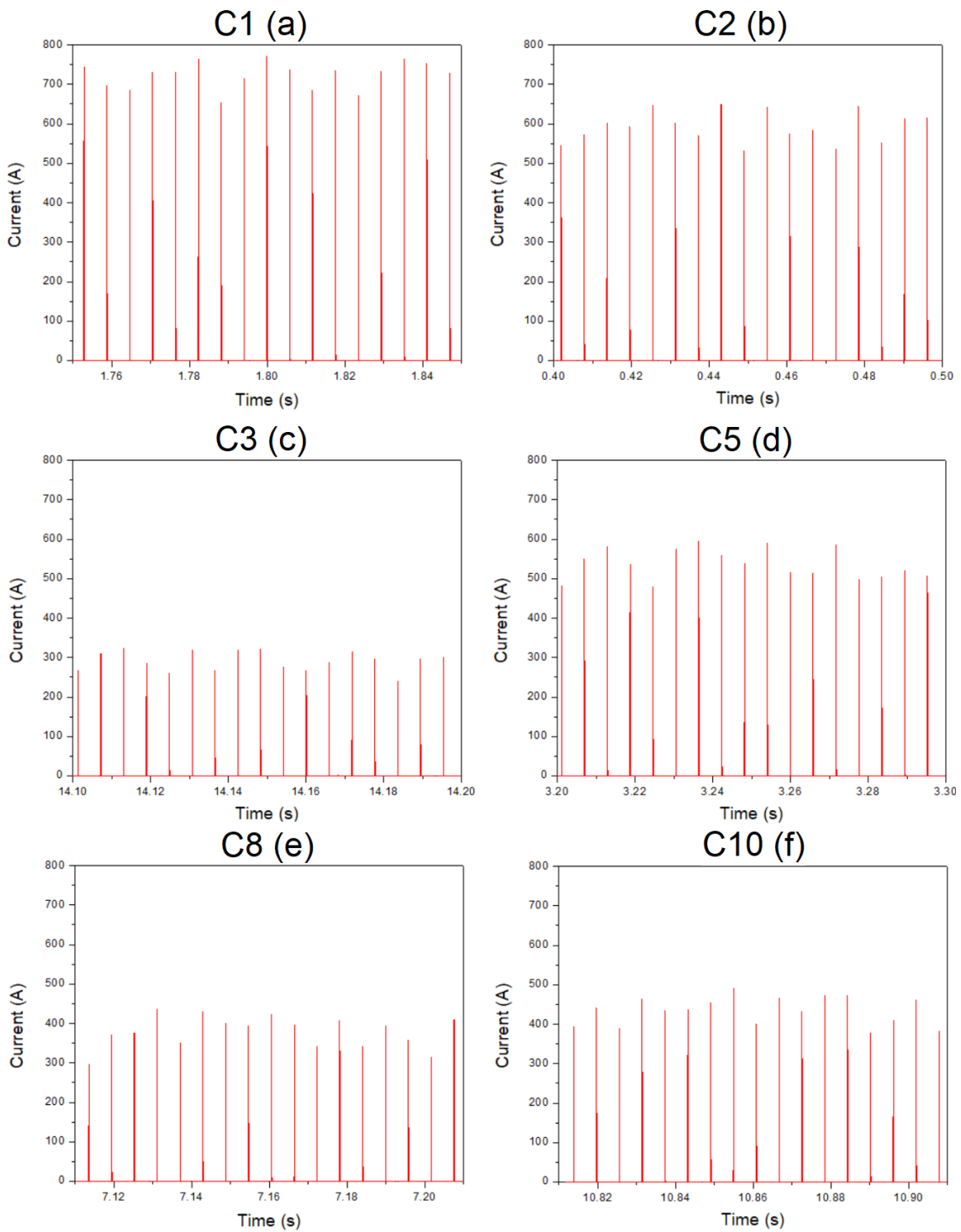
Figure 4.11: Pulses of current observed for the studied conditions in an interval of 0.1 second.

The average total energy observed for C10 is higher than C3, 124.47 J and 58.35 J respectively. These two conditions present an average area of defects close to each other, respectively 0.37% and 0.27%. The higher total energy of C10 may have contributed to a higher formation of defects when comparing to C3.

Table 4.4: Total energy for the conditions studied.

	C1	C2	C3	C5	C8	C10
Total Energy (J)	322.15 ± 9.33	225.62 ± 4.01	58.35 ± 0.79	195.95 ± 3.84	124.04 ± 2.37	124.47 ± 0.91

A small decrease in capacitance appears to have a slight consequence in defects when comparing C2 and C5, since both set of parameters have similar area of defects with huge variance and capacitance of respectively 120 µF and 100 µF, although the average total energy is higher for C2. A decrease of 50 µF in capacitance from C5 to C8 not only reduces the total energy for values 150 J, but also decreases the average I_{max}. A combination of lower total energy and lower average I_{max} may be the source of lower fraction of defects of C8 when comparing to C5.

Analyzing the results presented by Figure 4.6 and Figure 4.10, it seems that there is a threshold for a high fraction of defects in a deposited layer. In terms of pulse energy, average maximum current and total energy, it is observed that for pulse energy greater than 0.400 J, average peak current greater than 500 A and total energy greater than 150 J, the percentage of defects increases. With a combination of high pulse energy and high total energy, more electrode material is being melted, and considerably increase in scattering of material is expected to occur during the material transfer, contributing to an accentuated fraction of defects within deposited layers.

4.3.2 Microstructure and total energy of C1 and C2 with different spark frequency

Figure 4.12 shows representative optical micrographs of the deposited layers for C1 and C2 with different frequencies. The defects here observed have a similar form to those previously observed for the other conditions presented in the section 4.1, like voids and lack of fusion. For depositions made with frequencies of 85 Hz and 64 Hz, it is observed depositions with good homogeneity and with a few defects. With high frequency of 300 Hz, see Figure 4.12(d), C2 presented huge cavities and voids like those observed for C1 with frequency of 170 Hz, see Figure 4.3.
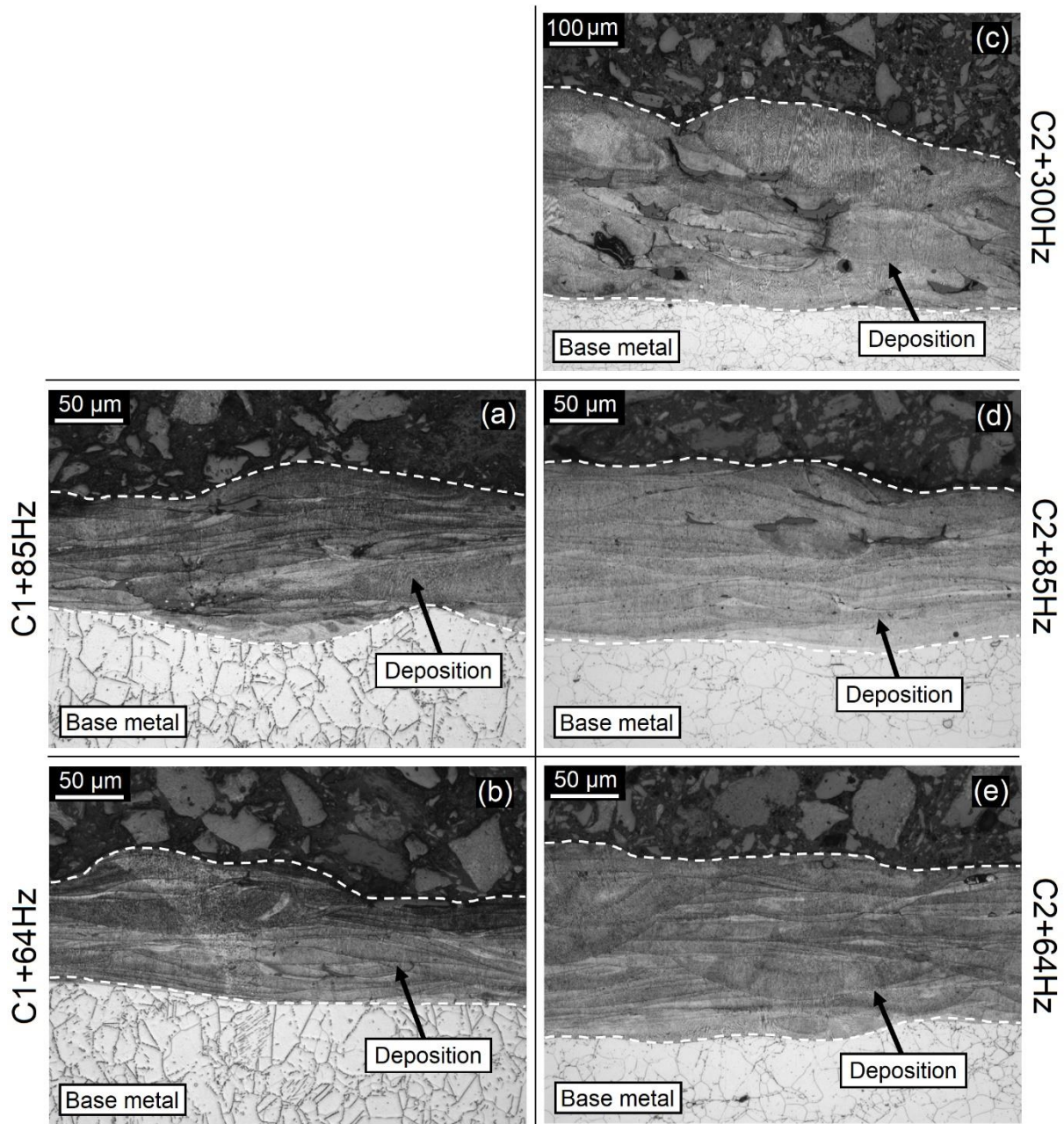
Figure 4.12: Optical micrographs showing cross-sections of the depositions for different conditions, which are within the dashed lines. Different scales are observed. Dark areas within the depositions are defects commonly observed. Oxalic acid 10% etchant.

Table 4.5 presents the thickness of the ESD deposited layer for C1 and C2 with different frequency. Table 4.6 shows the total energy for C1 and C2 with different frequency. The total energy seen in Table 4.6 is an average of the energy taken in three different periods of 0.1 seconds during the ESD process for each condition.

C1 presented a reduction in thickness when compared to the original deposition made with frequency of 170 Hz (343 ± 138 µm). A similar trend was observed for C2, when deposition made with 170 Hz reached thickness of 264 ± 45 µm, and with

reduced spark frequency the thickness of the deposited layers has been reduced. With an increase in spark frequency, for example C2 from 85 Hz to 170 Hz, the amount of mass ejected away from the electrode onto the substrate within a fixed interval of time is increased, augmenting the thickness of the deposited layer [56]. With increased frequency of 300 Hz, C2 presented a similar thickness to that of the layer made with 170 Hz.

Table 4.5: Thickness of the deposited layers for C1 and C2 with different frequency. The values for C1 and C2 with frequency of 170 Hz are shown again here for comparison.

	C1 170Hz	C1 85Hz	C1 64Hz	C2 300Hz	C2 170Hz	C2 85Hz	C2 64Hz
Thickness (µm)	343 ± 138	110 ± 14	103 ± 24	261 ± 53	264 ± 45	120 ± 15	126 ± 20

The total energy input per a fixed interval of time can also be modified by varying the frequency. The total energy observed for C2 with a pulse frequency of 170Hz is 225.62 ± 4.01 J, while the total energy for C2 with a pulse frequency of 300Hz is 397.75 ± 2.28 J. An increase in the energy being transferred during the process, in each given interval of time, may have increased the vaporization and scattering of the material of the electrode during the material transfer, contributing to a deposition that showed thickness similar to a deposition made with lower pulse frequency and consequent lower total energy [48].

Table 4.6: Total energy for C1 and C2 with different frequencies. The values for C1 and C2 with frequency of 170 Hz are shown again here for comparison.

	C1 170Hz	C1 85Hz	C1 64Hz	C2 300Hz	C2 170Hz	C2 85Hz	C2 64Hz
Total energy (J)	322.15 ± 9.33	163.82 ± 3.81	131.05 ± 3.45	397.75 ± 2.25	225.62 ± 4.01	116.16 ± 2.86	83.55 ± 1.37

Moreover, it is observed that a high pulse energy with a low spark frequency can be used to obtain a thick coating with lower percentage of defects, as noted for C1 and C2 using 64 Hz for depositions [1].

4.3.3 The fraction area of defects

Figure 4.13 presents the percentage of defects for Condition 1 (C1) and Condition 2 (C2) using different frequencies. It is possible to observe in Figure 4.13(a)

and (b) that the fraction of the defects in the deposited layer is reduced with the reduction in spark frequency for both conditions.
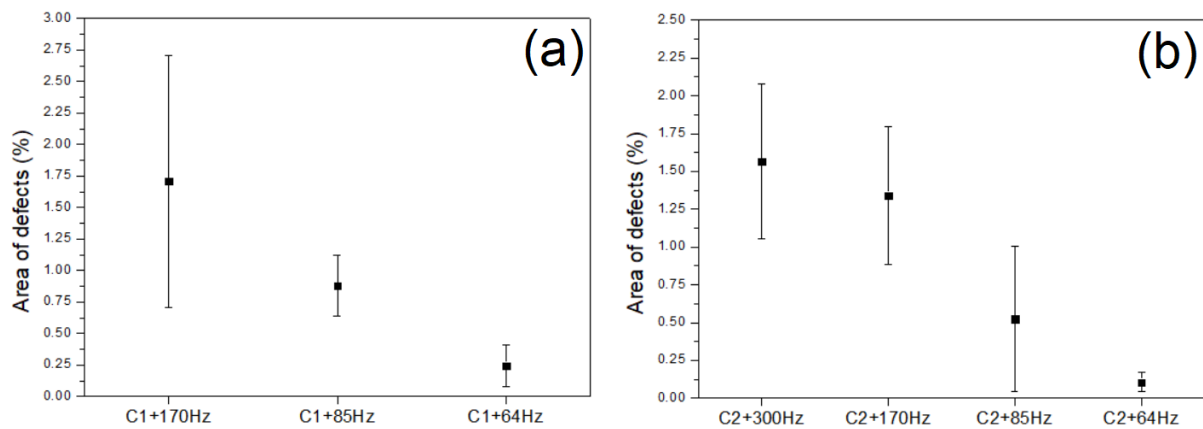
Figure 4.13: (a) area of defects for C1 with different frequencies. (b) area of defects for C2 with different frequencies. The values for C1 and C2 with frequency of 170 Hz are shown again here for comparison.

Heat is released during the spark discharge, and the volume of liquid phase formed in the electrode is a function of several factors. One of which is the temperature difference ($T_m - T_0$) between the melting point (T_m) of electrode material and its initial temperature (T_0) [56]. With the application of more pulses in the same period, it would be possible that during the deposition with higher spark frequency a condition where the temperature T_0 of the electrode started to increase from pulse to pulse, increasing the volume of the melted material. As discussed before, an increase in total energy may contribute to a considerably increase in melting and posterior scattering of material during the transfer, with a corresponding increase in the formation of defects within the ESD deposited layers, as observed in this section when deposition using C1 and C2 were performed with higher spark frequency.

4.3.4 Roughness

Figure 4.14 presents topographies of the samples after ESD deposition using different conditions. Table 4.7 shows the surface roughness (R_a) and the peak-to-valley height (R_z) of ESD coated IN718 with different conditions.
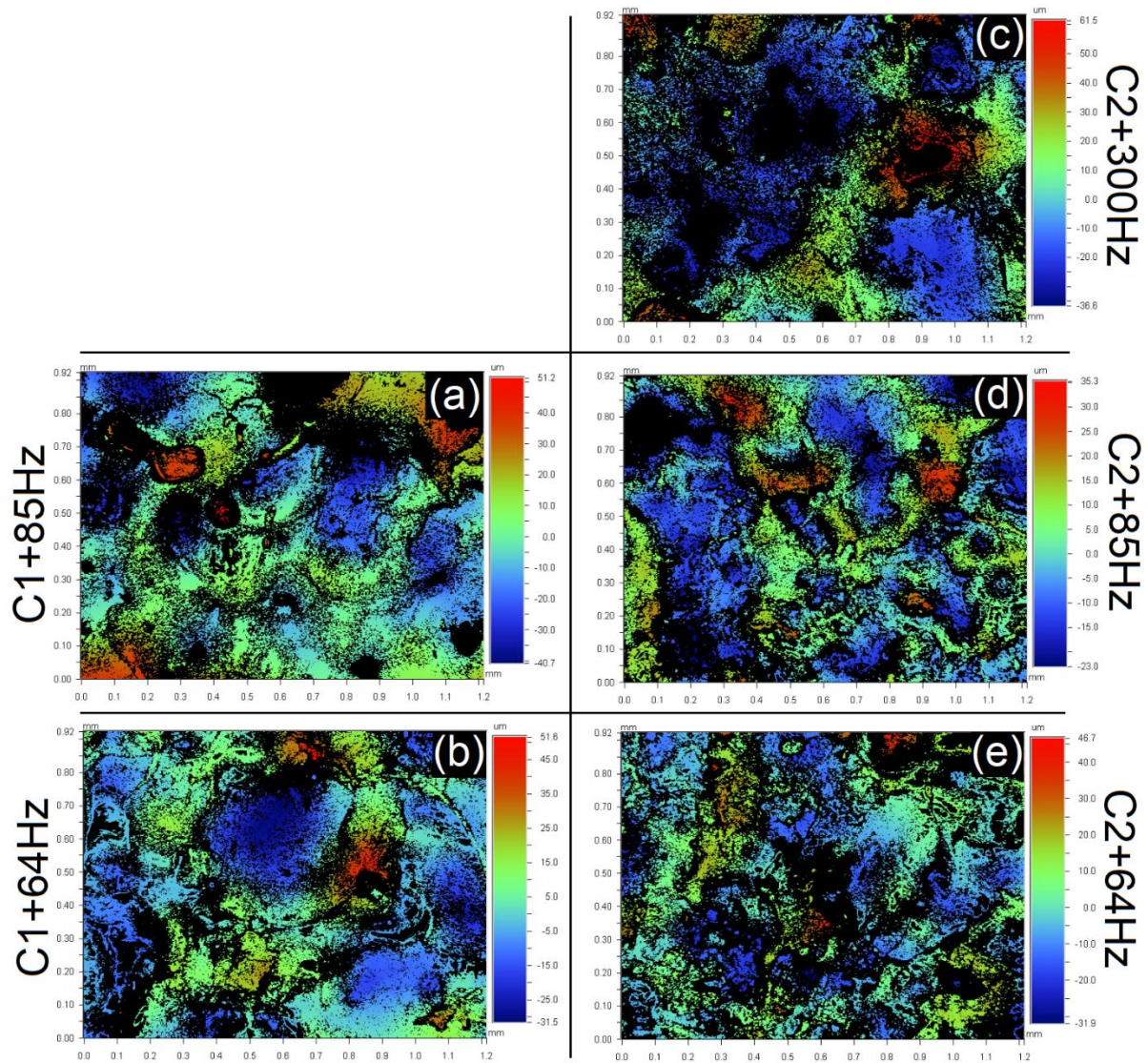
Figure 4.14: Topography of the surfaces for C1 and C2 with different frequency. Note the difference in scale within the color map. Dark areas are regions that exceed the range of measurement of the equipment.

Table 4.7: Surface statistics for the conditions studied. The values are an average of three measurements over the deposited layers. The values for C1 and C2 with frequency of 170 Hz are shown again here for comparison.

	C1 170Hz	C1 85Hz	C1 64Hz	C2 300Hz	C2 170Hz	C2 85Hz	C2 64Hz
R_a (µm)	16.11 ± 2.50	10.69 ± 0.98	8.88 ± 1.23	15.19 ± 0.79	13.57 ± 2.61	8.67 ± 0.77	8.52 ± 1.00
R_z (µm)	112.66 ± 26.96	87.77 ± 3.92	77.55 ± 5.99	100.69 ± 9.63	96.33 ± 7.51	67.60 ± 12.46	79.73 ± 13.75

It is observed in Figure 4.14 and Table 4.7 that there is an increase in roughness and peak-to valley distances as the pulse frequency increase. This may be

explained since more material is being melted in a deposition with higher pulse frequency and consequent total energy. This may contribute to an uneven distribution of material during the scattering, which will lead to an accentuated formation of defects, like voids, within the deposited layer of high frequency depositions, as observed in Figure 4.13, since the molten material may not reach the bottom of the deep cavities or and craters, forming cold laps, voids or insufficient fusion.

4.4   Summary

In this chapter, a comprehensive analysis was performed in order to suggest mechanisms that explain the formation of defects during the ESD coating made with different pulse energies and pulse frequency. Moreover, a correlation between the pulse energy and pulse frequency with the fraction of defects and roughness of samples was presented. Based on the experimental observations, the area fraction of defects increases with increased pulse energy and total energy. It is notable that the deposition rate increased with increasing pulse energy and spark frequency. A corresponding increase in roughness is observed for an increased pulse energy and pulse frequency.

5. Chapter 5 – The microstructure and mechanical properties of the Electrospark deposited IN718

In this chapter, the microstructure and mechanical properties of ESD repaired IN718 with different pulse energy will be discussed.

5.1 The microstructure evolution of the ESD deposited IN718

The microstructure of the deposited layers can be observed in Figure 5.1. The solidified microstructures for all depositions consist of cellular growth, with a microstructure that suggests grains epitaxially grown from the substrate and from previous splats boundaries, a growth that has been reported in the literature for ESD microstructures [18, 40, 57]. The cooling rate of the ESD process may reach values in the order of 10^5 to 10^6 K/s [5, 18]. The rapid solidification of the deposited material in the form of small dimensions splats in a very short time is believed to induce the formation of constitutional supercooling, which is responsible for the promotion of the cellular solidification mode [40, 58].

Figure 5.1(a) shows a microstructure that suggests cellular grains with different cell spacing, with finer spacing on the top of the figure, where the subsequent splat solidified. The cell spacing differs within the deposited layers of the three specimens studied, indicating different cooling rates along the deposited layers [42]. Coarse particles are present in the deposited layers, like the dark areas presented in Figure 5.1(a), (e) and (f) and precipitates pointed by arrows in Figure 5.1(c).
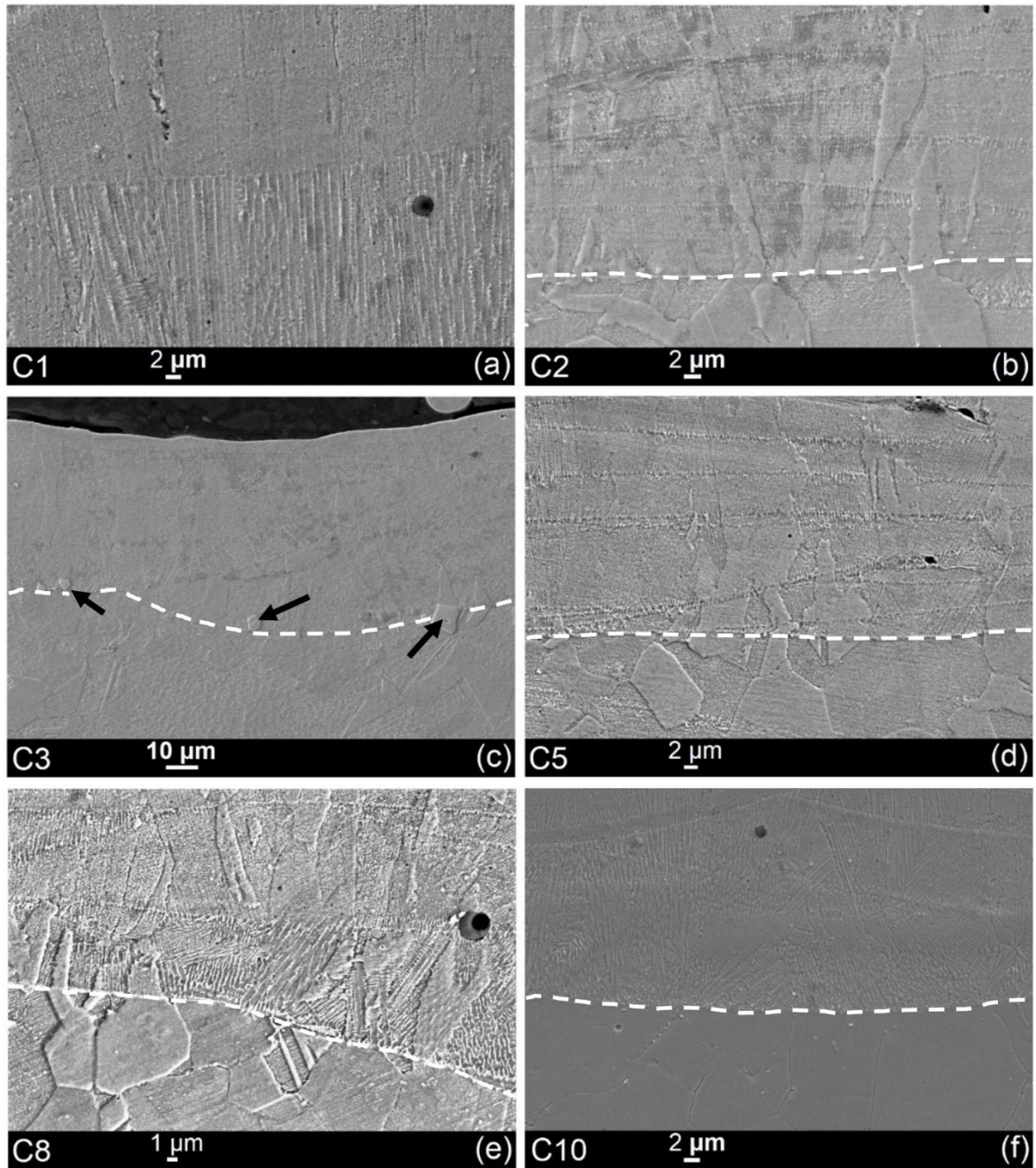
Figure 5.1: Microstructure of the deposited layers of six conditions studied presented with different magnifications. Niobium-rich precipitates are pointed by arrows in (c). Inverted glyceridea etchant, except for microstructure of (f), revealed using Oxalic acid 10%. Different scales are observed. Dashed lines indicate the boundary base metal-deposition, with shown deposition in the upper part of the figure.

Figure 5.2 shows optical micrographs of the depositions made with C1, C2 and C3 where the columnar grains epitaxially grown from the substrate are observed. Although not shown in Figure 5.2, it should be noted that similar microstructures are observed in all samples of this study.
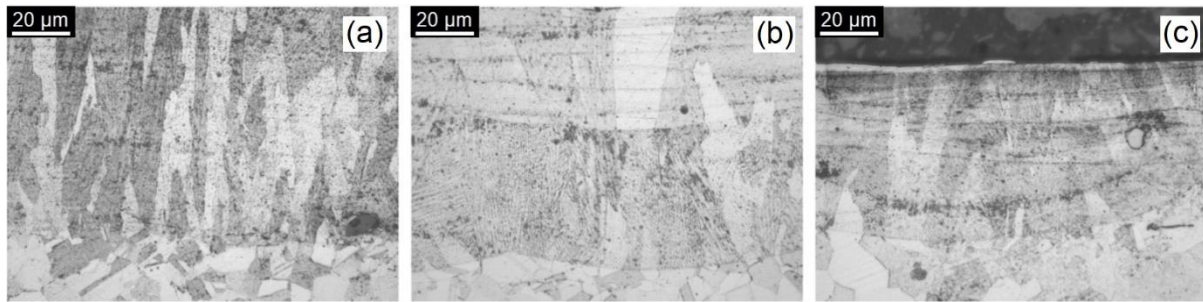
Figure 5.2: Micrographs taking at higher magnification, to reveal the microstructure, of the C1, C2 and C3 depositions shown in (a), (b), and (c) respectively.

The chemical analysis performed on the central precipitates (arrowed) of Figure 5.1(c) indicates the formation of niobium-rich precipitate within the ESD deposited layer of IN718, as can be observed in the EDX spectrum shown in Figure 5.3(b).
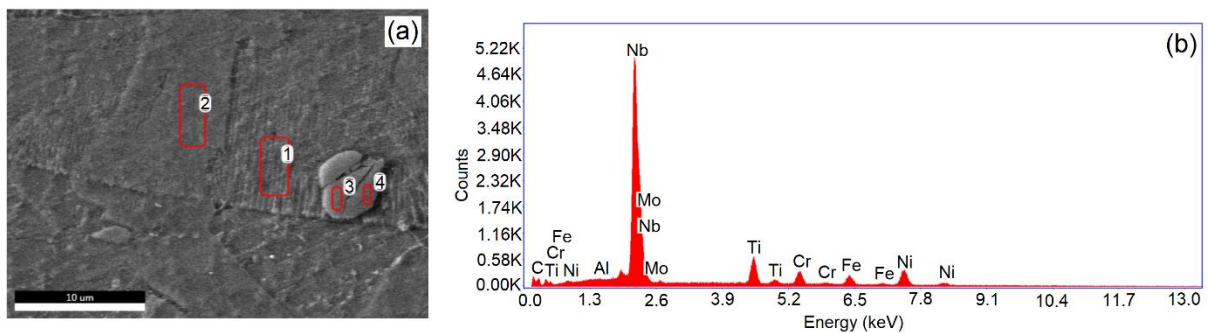
Figure 5.3: (a) Niobium-rich precipitate formed within the ESD deposited layer of IN718 close to the interface deposition-base metal. (b) EDX spectrum of the area 3 showing a strong diffraction of niobium.

There are three major boundaries observed in the ESD deposited layers of IN718: the fusion boundary between substrate and deposition, the fusion boundaries between splats and the grain boundaries within the microstructure, as shown in Figure 5.4(a). The fusion boundary between the base metal and deposition is perpendicular to the build-up direction, the same is observed to the fusion boundaries between splats. Grain boundaries are parallel to the build-up direction, with grains varying in shape and showing competitive growth within the deposited layers. Figure 5.4(b) displays an area with higher magnification of Figure 5.4(a). The epitaxial solidification is noticed in the fusion boundary, with similar tendency observed in Figure 5.1 and Figure 5.2. A continuous fusion boundary has been observed in most of the interface deposition-base metal, although defects like lack of fusion are also observed in small areas like that observed in Figure 5.4(b). Coarse particles of secondary phase are depicted in Figure 5.4(b).
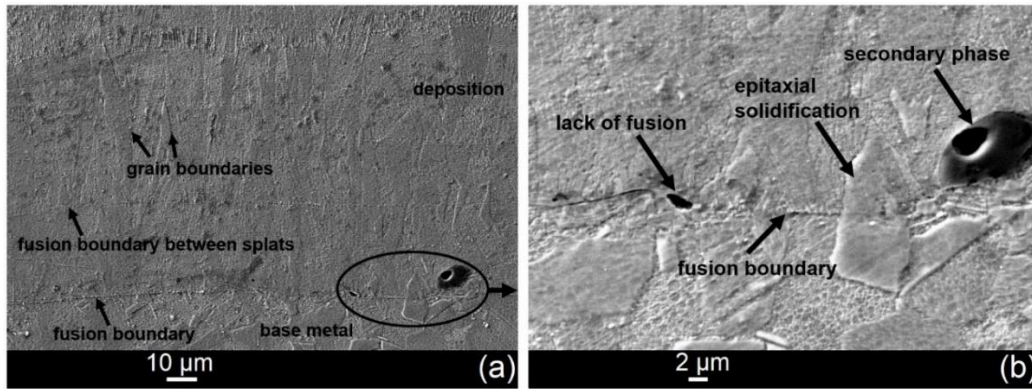
Figure 5.4: SEM images showing the deposited layers of highest pulse energy: (a) overall microstructure of the deposited layer, (b) higher magnification showing fusion boundary and segregation of second phase. Inverted glyceridea etchant.

Those relatively coarse intermetallic precipitates are often observed within the ESD deposited layers with morphology that are different from those commonly found in the IN718 substrate. Elemental mapping of one of these intermetallic particles is presented in Figure 5.5, where is observed that they are rich in Al, Ti, and Cr but contain very minimal amount of Ni, Nb, Fe, Mo.
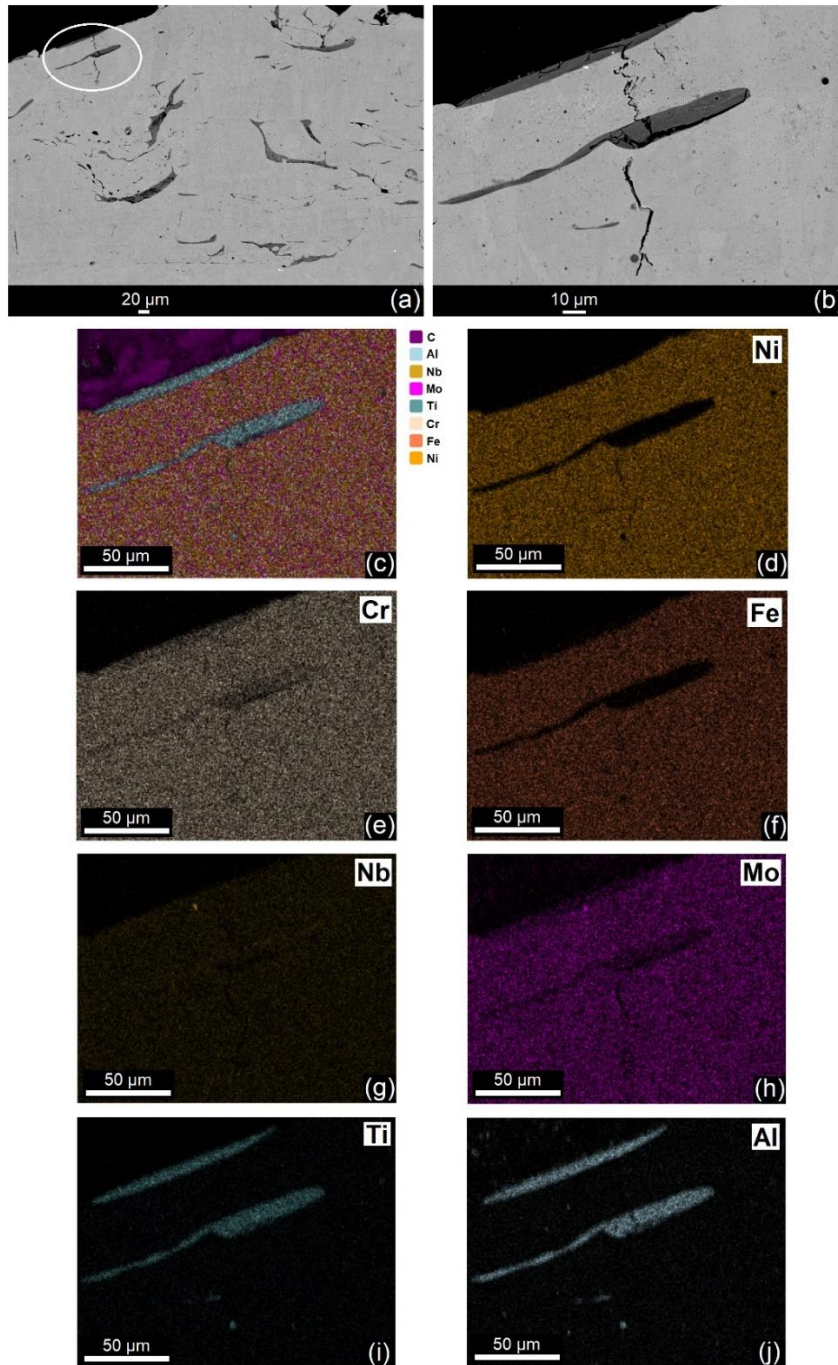
Figure 5.5: (a) and (b) Backscattered SEM images of deposition 1 showing elemental contrast, indicating the formation of segregation. (c) to (j): elemental distribution in the area correspondent to (b).

Specific point and ID analyses of the particle showed in Figure 5.6(b) yielded an elemental composition of approximately 18-23wt.% Al, 28-31wt.% Ti, 25-32 wt.% Cr, 2.0-2.15 wt.% Ni, and 8-12wt.% Nb, as can be observed in Figure 5.6.

Figure 5.6: (a) intermetallic precipitate observed in ESD deposited IN718 and its respective elemental composition in (b).
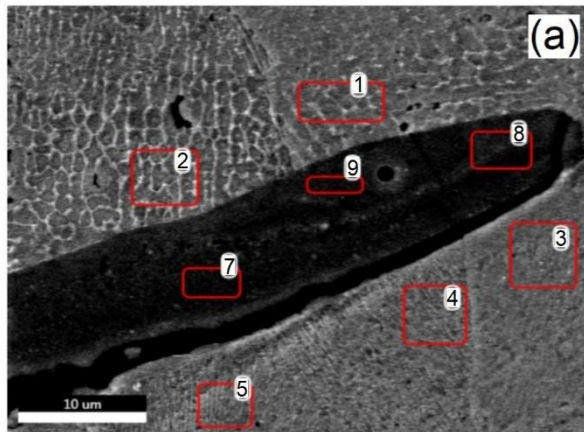
Area	Al	Ti	Cr	Ni	Nb
Area 7	21.42	34.82	25.60	2.08	8.14
Area 8	18.51	28.56	31.23	2.14	11.37
Area 9	22.23	31.27	27.73	2.09	8.64

The small presence of Ni in the intermetallic precipitates suggests that the precipitation of nickel-rich phases, such as the fcc γ' ($Ni_3(Al,Ti)$), the bct γ'' (Ni_3Nb), the orthorhombic δ (Ni_3Nb) and the hcp η (Ni_3Ti), commonly found in IN718 are unlikely to be responsible for the formation of these coarse intermetallic particles observed here [12, 59]. In addition, the elements identified via elemental analysis did not match other known topologically closed packed (TCP) phases frequently found in solidified IN718. It is important to note that there are some similarities to the laves phase, generally accepted to be in the form of $(Fe,Cr,Mn,Si)_2(Mo,Ti,Nb)$ [12, 26, 27], notwithstanding there are some considerable differences. For example, common laves phase observed in solidified IN718 usually contains a significantly higher content of Ni and Nb [60], which the absence of mainly the former element is peculiarly observed here in the intermetallic particle. Moreover, Al are rarely reported to be in such a large quantity within the laves phases, although these intermetallic are rich in Al.

Furthermore, the geometry and morphology of the intermetallic are also notably different from the typical plate geometry of the laves phase found in IN718. The intermetallic particles are rather large and are often found lining the interfaces between the individual ESD splats. The area fraction and by consequence the volume fraction of these intermetallic particles tends to increase with increasing pulse energy as shown in Figure 5.7.
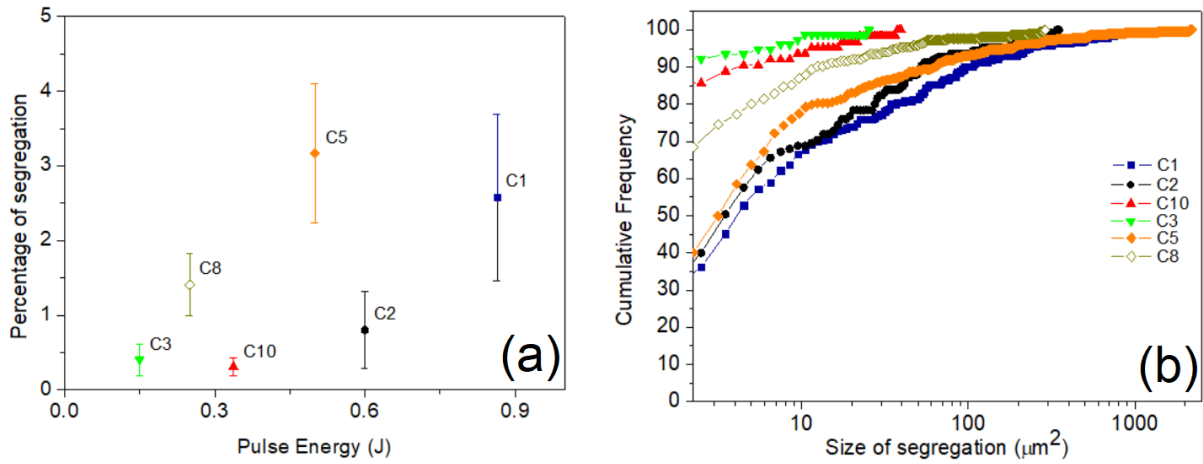
Figure 5.7: (a) Relationship between the area fraction of intermetallic segregation versus the pulse energy used in each deposition. (b) Cumulative distribution of the intermetallic segregation for all conditions.

Additionally, the pulse energy has likewise a comparative effect on the average size of the intermetallic particles also as the largest particles observed, as shown in Figure 5.7. In this work, the intermetallic are likely to be considered non-equilibrium phases, like the TCP phases in superalloys, and the dependence on the pulse energy is linked through the overall heat input onto the deposition, and more significantly the rapid cooling rate achieved as a result. It is suggested in the literature that the reduction on heat input and consequently increase on the cooling rate in the fusion zone significantly refines and reduces the size and amount of intermetallic like laves in solidified microstructures of IN718 [30, 51]. More study will be required to accurately determine the identity and origin of these intermetallic particles. Their presences are expected to be detrimental to the ductility and fracture properties of the ESD layers due to its inherent brittle nature, similar to the TCPs in IN718 [12, 30].

Moreover, the precipitation of intermetallic with a variety of forms is observed in the ESD depositions of IN718 made with all the conditions studied, as can be observed in the elemental mapping depicted by Figure 5.8.
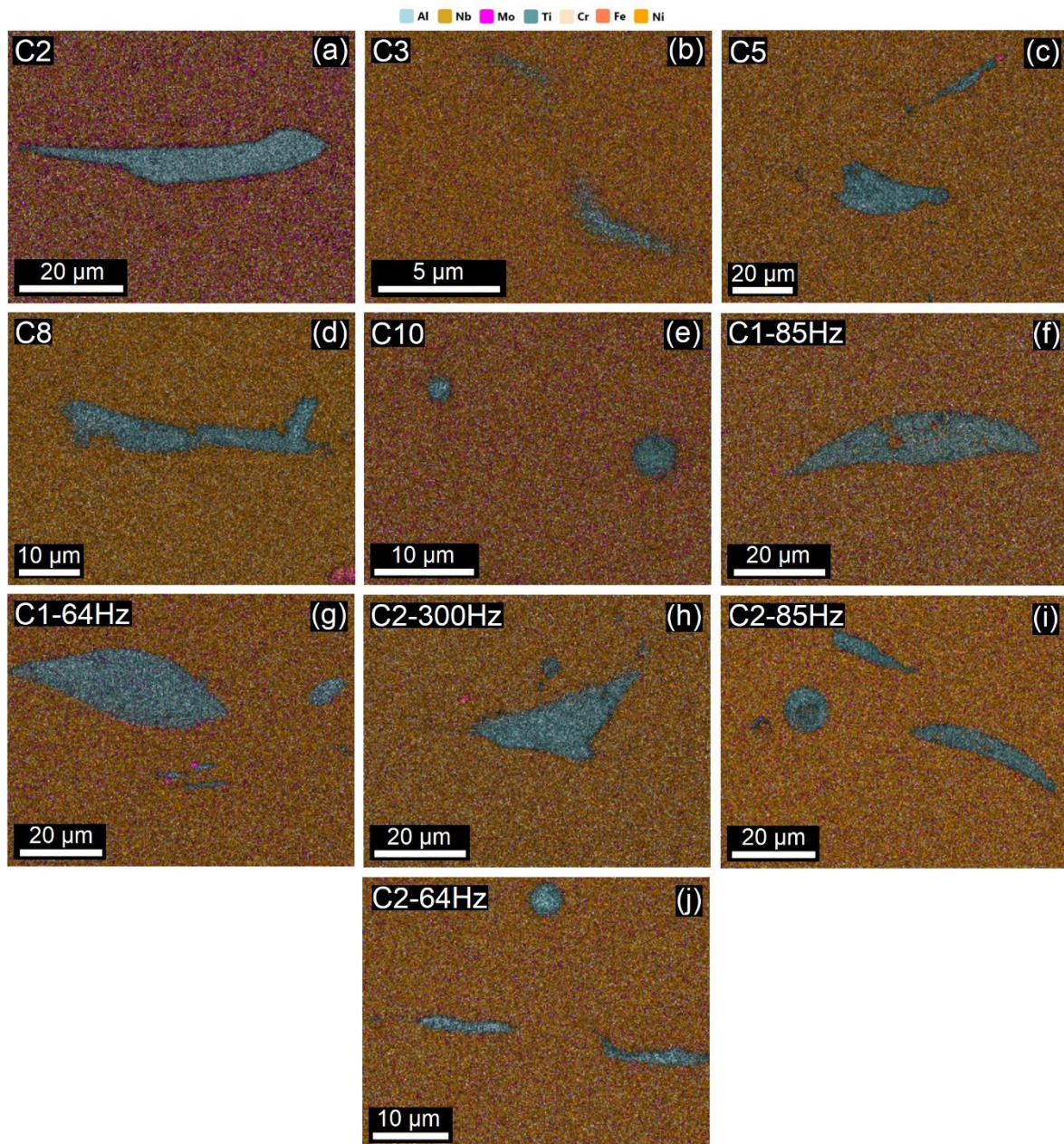
Figure 5.8: Intermetallic precipitates observed in depositions made with different conditions. C2, C3, C5, C8 and C10 were depositions made with 170 Hz.

The area fraction of the observed intermetallic particles is likely to increase with increasing total energy, as revealed by Figure 5.9 for depositions made with different pulse frequency. C2+85Hz and C2+170Hz are considered anomalies considering that all other samples show a general trend that indicates an increase in area fraction of intermetallic with increased pulse energy and total energy. The variation in the percentage of intermetallic may be explained by the random nature of the formation of

these intermetallic during ESD process which has a formation mechanism that requires more research to be understood and clarified.
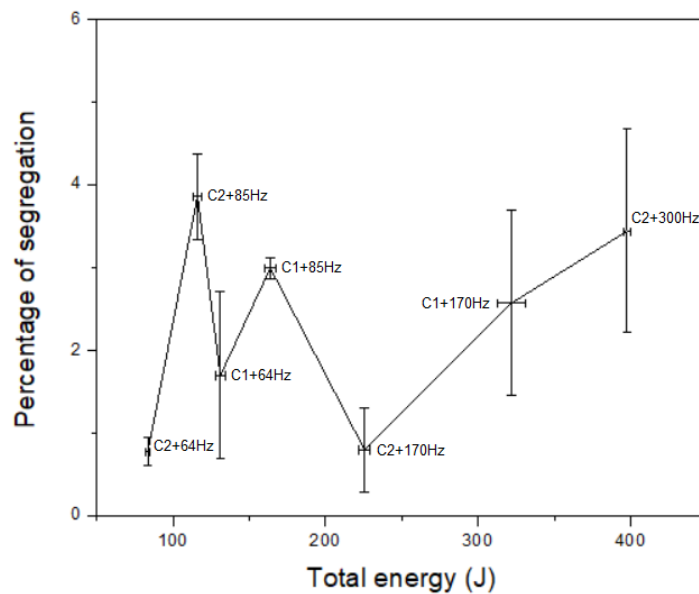
Figure 5.9: Relationship between the area fraction of intermetallic segregation versus the total energy within a 0.1 second window for C1 and C2 with different spark frequency.

5.2   Microhardness of the ESD deposited IN718

Figure 5.10 shows the microhardness along the deposited layers of samples after deposition made with C1, C2 and C3, as well as microhardness for the base metal in the interface with the deposition. It is observed that the microhardness of ESD deposited layers is similar to that observed for the base metal. It is suggested in the literature that strengthening phases like carbides or other phases that form within the deposited layers may considerably increase the hardness of the ESD deposited layers [5, 39, 4, 43]. In the ESD deposited IN718, the microhardness of the coarse intermetallic is much higher than the deposition, as can be seen in Figure 5.10(a), where one of the indentations hit an intermetallic particle and presents hardness of 1734 HV.
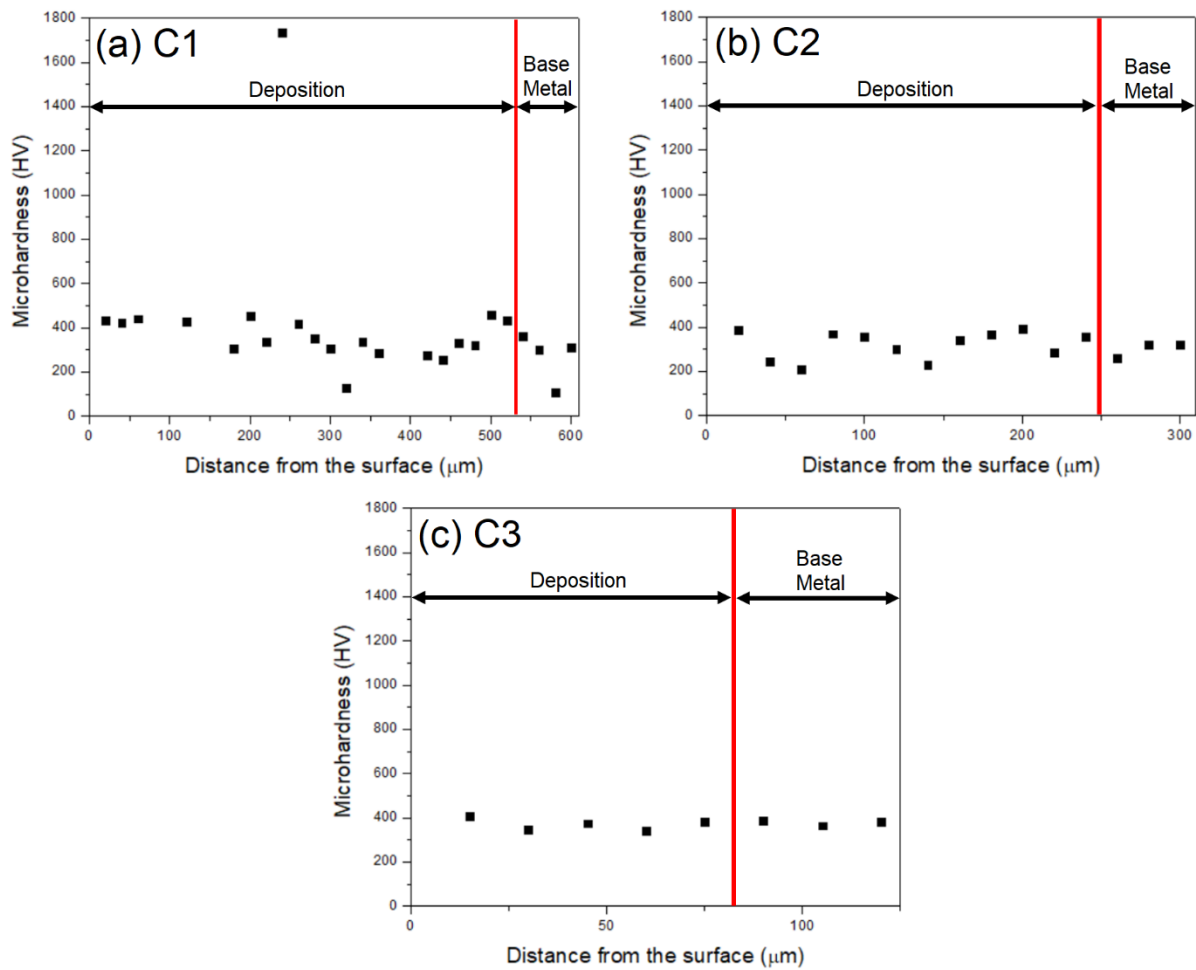
Figure 5.10: Microhardness along the ESD deposited layer for depositions made with C1, C2 and C3. The load force is 10 gf.

5.3 Mechanical properties of ESD repaired IN718

The tensile properties of the ESD repaired samples can be observed in Table 5.1. It is observed that there are no major differences in the yield stress and Ultimate Tensile Stress (UTS) of the tested samples. Notched samples presented a slightly higher yield stress in comparison to the base metal because of notch effect that tends to amplify the stresses around the notch, increasing the resistance for yielding. Figure 5.11 presents the ranges for yield stress and ductility in function of the total energy for the tested samples.

The Notch strength ratio (NSR) is the ratio of nominal UTS of notched sample to UTS of unnotched sample, and NSR >> 1 means notch strengthening, while NSR << 1 means notch weakening, and NSR ~ 1 indicate that the strength of the material is insensitive to the designed notch [61]. In this work, the average NSR was found to

66

be 0.959 for the designed notch used in this study, which suggests that the strength of the bulk material is insensitive to notch.

Table 5.1: Tensile properties of the ESD repaired samples.

	C2	C2+64Hz	C10	Base Metal	Notched samples
Yield stress (MPa) (0.2%strain)	513.93 ± 27.66	519.40 ± 14.71	499.23 ± 23.59	526.52 ± 11.86	539.57 ± 22.96
UTS (MPa)	867.63 ± 23.64	871.35 ± 10.82	869.13 ± 19.60	893.17 ± 16.39	856.80 ± 1.66
Ductility (%)	32.09 ± 2.66	36.51 ± 0.05	35.97 ± 4.27	47.36 ± 1.63	28.34 ± 2.37

On the other hand, a major difference is observed in the ductility of the samples after repairing when comparing to the ductility of the base metal. A reduction in ductility more than 23% is observed. Notched sample presented the lower ductility because the stress concentrations in notched samples constrain the plastic deformation mainly in a small plastic zone, decreasing ductility [61].Those samples repaired with the condition with more internal defects (C2), presented ductility closer to the notched samples, respectively 32.09% and 28.34%. Samples repaired with the condition that showed less defects, C2 with a lower frequency of 64 Hz (C2+64Hz), presented ductility closer to the ductility observed for the base metal, respectively 36.51% and 47.36%. An increased number of defects within the repaired samples using C2 may have contributed to the nucleation and propagation of fracture that reduced ductility when compared to the samples repaired with C10 and C2+64Hz, that show microstructure with lower internal defects. The internal flaws like voids and delamination are points where stresses are magnified due to the local stress

concentration effects, locally lowering the strength and triggering fracture more easily [62].
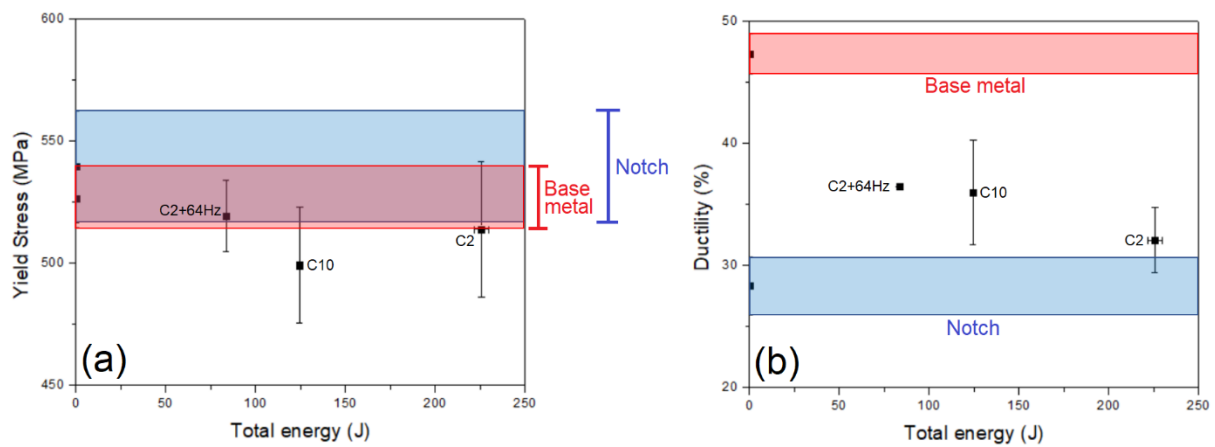
Figure 5.11: Ranges for yield stress and ductility for the tested samples. Shaded areas represent the ranges for notched sample and base metal.

A typical stress-strain curve for the repaired samples, notched and base metal is presented in Figure 5.12. The results presented in Figure 5.12 reveal that the presence of a notch and the ESD repairing of samples dramatically decreased the elongation of the tested samples.
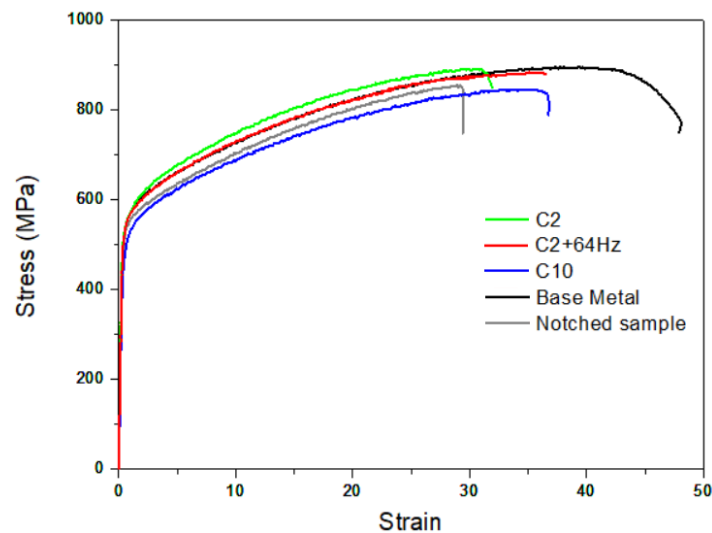
Figure 5.12: Stress vs. strain curves for samples closer to the average ductility of each condition.

Figure 5.13 presents stereoscope images of the samples after tensile tests. The repaired samples fractured in the middle of the sample in the repaired region, with the notched samples presenting a similar trend. It is observed in (d) that the base metal

samples fractured in a region far from the center, presenting a cup and cone fracture with visible shear lips, which indicates a ductile fracture.
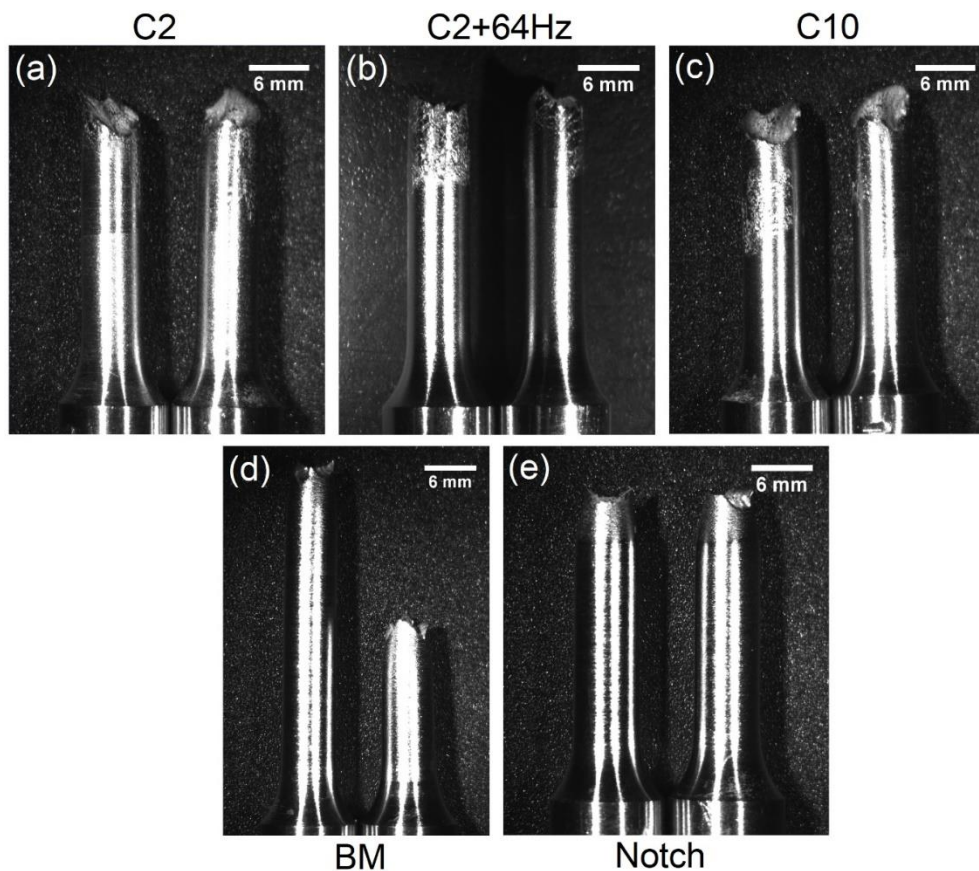
Figure 5.13: Stereoscope images showing the samples after tensile tests.

The fracture surface of the samples close to the edge can be observed in Figure 5.14. The fracture surface of the condition C2 is characterized by multiple secondary cracks and delamination in comparison to the other samples repaired with conditions that present a lower percentage of defects within the deposited layers, C2+64Hz and C10, that can be observed respectively in Figure 5.14(b) and (c). The accentuated percentage of defects combined with the presence of intermetallic particles within a C2 deposition may have contributed to the nucleation and propagation of cracks within the deposited layer under stresses. The precipitation of intermetallic phases may degrade the ductility of high-strength high-temperature alloys, like the IN718, because this secondary phase creates preferential sites for crack initiation and propagation [12, 30].

The base metal and notched samples presented dimples on the fracture, indicating a ductile fracture, as can be seen correspondingly in Figure 5.14(d) and (e).
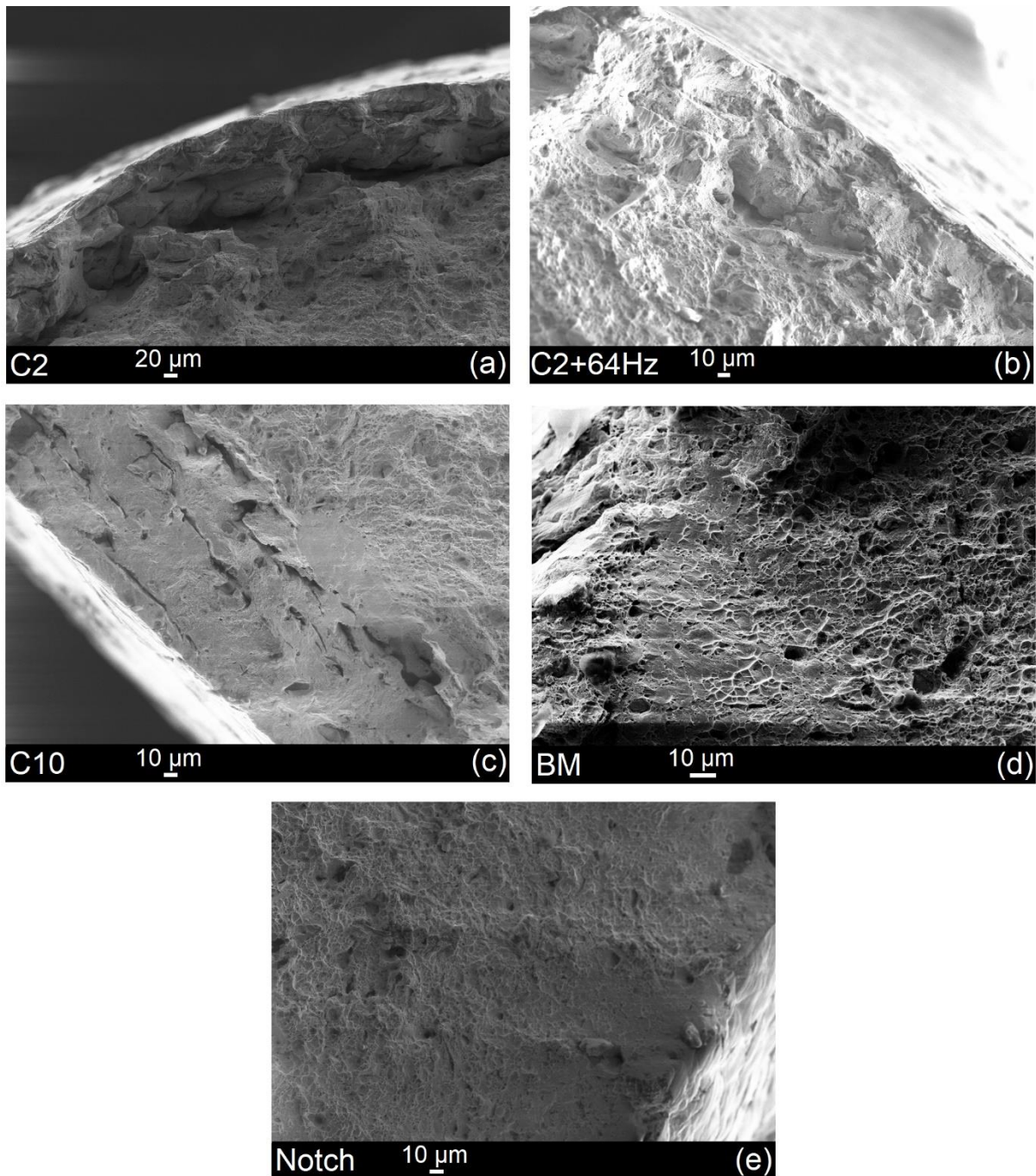
Figure 5.14: Fracture surface of the samples close to the edge.

The crack appearance of the repaired region observed in Figure 5.15(a) for C2 suggests that the crack propagated in a mixed intergranular and transgranular mode. A similar fracture mode was observed in IN718 tensile samples manufactured by selective laser melting technique, when the crack path suggests a mixed mode indicated by the appearance of intergranular grain facets and intragranular surfaces, while the microstructure of the samples presented a cellular-dendritic microstructure like the microstructure observed for ESD repaired samples in this work [63]. The

jagged fracture surface of C2 in the deposition region suggests that the increased amount of internal defects and intermetallic contributed to the propagation of secondary cracks that eventually reached together to a major crack that leaded the sample to failure. Secondary cracks, like that indicated in Figure 5.15(c), are also observed in the fractures of the samples repaired with C2+64Hz and C10, but it seems that these secondary cracks that may be nucleated in preexisting inter-splat delamination did not divert the path of the main crack. Shallow dimples are commonly observed in fractures of the samples repaired with C2+64Hz and C10, suggesting that the fracture occurred in a more ductile mode. The dimpled appearance of some regions of the fractures suggest that the fractures absorbed more energy during the failure process, which may have contributed to an increased ductility of the samples repaired with C2+64Hz and C10 in comparison to those repaired with C2.
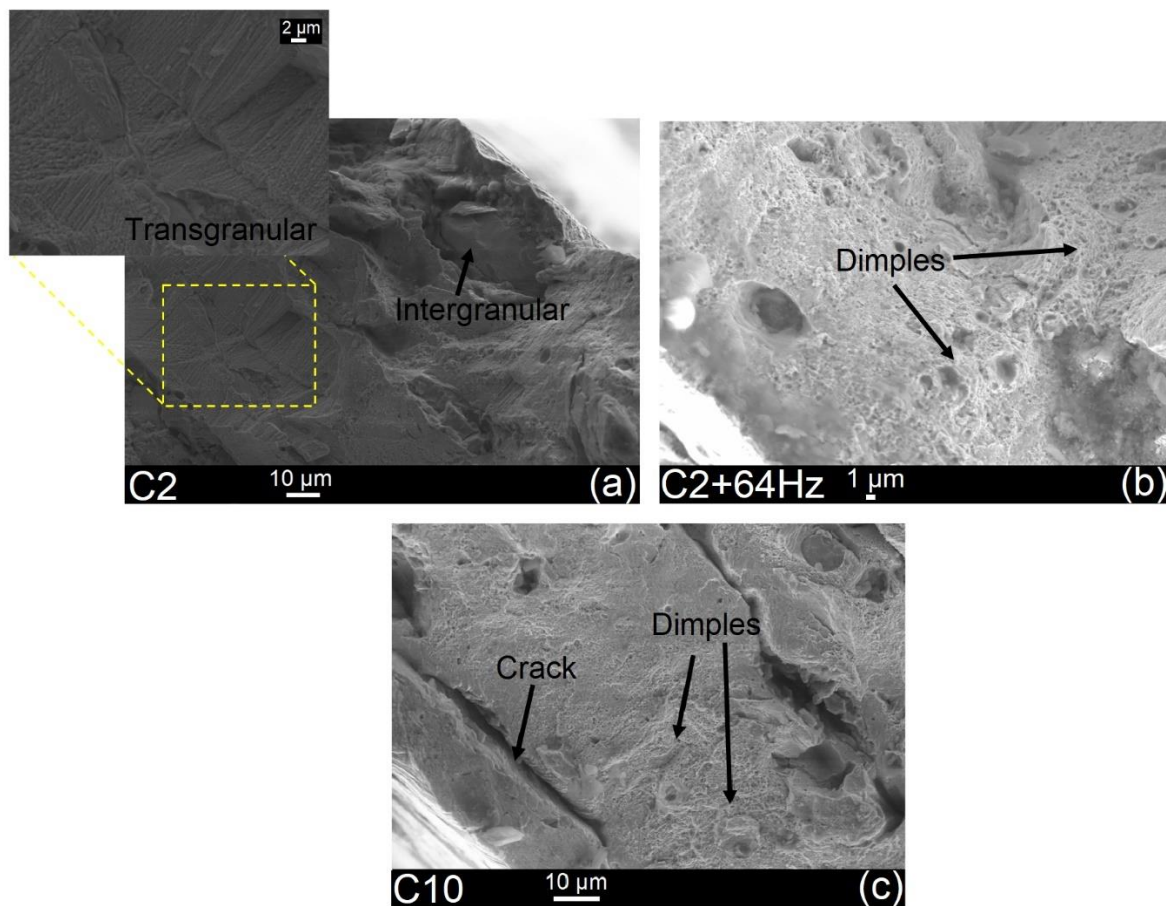
Figure 5.15: Fracture surface of the samples showing the fracture mode for different conditions.

5.4   Summary

In this chapter, the microstructure, the microhardness and tensile properties of ESD repaired IN718 was presented and discussed. The microstructure of all depositions consists of cellular with grains epitaxially grown from the substrate and from previous splats. The presence of secondary phases like Nb-rich precipitates and intermetallic phases rich in chromium, aluminum and titanium were observed for all conditions studied. Microhardness of the depositions was kept constant along the thickness of the coating and are analogous to the microhardness of the base metal. Repaired samples showed a minor difference in the yield stress for different conditions and presented a slight increase in ductility for samples repaired with conditions that show reduced internal defects.

6. Chapter 6 – Conclusions and recommendations

In this chapter, major observations and outcomes about the ESD repaired IN718 are presented, along with conclusions and recommendations for future work based on the results and conclusions achieved during this thesis.

6.1 Conclusions

After studying the influence of pulse energy and frequency on the microstructure and properties of ESD repaired IN718, the following conclusions are drawn:

1) Higher pulse and total energy used in the ESD process promotes the formation of deposited layers with high variance in thickness. An uneven distribution of molten material is expected to increase with augmented pulse and total energy, increasing the formation of defects like cold laps, voids and insufficient melting;

2) Deposition made with high pulse energy and low spark frequency presented a reduction in the fraction of defects when comparing to deposition made with high pulse energy and higher frequency. The results presented an increase in deposition quality when high pulse energy was combined with low pulse frequency, inducing a low input energy with possibly lower temperature on the tip of the electrode, which is expected to influence the melting and consequently scattering of materials, reducing internal defects;

3) The surface roughness of ESD deposited IN718 tends to be higher with increasing pulse and total energy. The high surface roughness of the ESD deposited IN718 may prevent the rotating electrode from approaching the bottom of deeper craters for sparking to occur and hence will contribute to the formation of defects such as insufficient fusion within deposited layer;

4) Relatively coarse intermetallic particles were observed within ESD deposited layers of IN718, and the presence of coarse second phases particles is diminished with reducing pulse energy and total energy. The reduced heat input and high cooling rate of depositions with lower energy is believed to reduce the size and amount of intermetallic in solidified microstructures. The presence of brittle intermetallic phases promoted the formation of cracks in the vicinity of the particle, particularly in depositions performed with higher energy;

73

5) Tensile tests produced small differences in the yield stress and ultimate tensile stress of the repaired samples in comparison to the base metal and notched sample. A slight reduction in terms of ductility is observed for the samples repaired with the condition that produces more defects, Condition 2 (C2), since this condition showed ductility closer to the notched samples. Samples repaired with low area fraction of defects, conditions C2 with lower pulse frequency (64Hz) and C10, produced ductility closer to the base metal. It is observed a fracture surface with more secondary cracks and delamination on the surface of the samples repaired with C2. This may have contributed to a lower ductility in those samples.

6.2 Recommendations for future work

The following statements are proposed as future work after the investigations and conclusions done in this thesis:

1) A further study of the influence of the microstructure of the substrate in the formation of the spark is necessary, since the electrical properties of a finer microstructure may influence the formation of a spark and consequently the material transfer mode;

2) A better understanding of the material transfer mode during the ESD process, since this process may influence the scattering and impingement of material during deposition;

3) The nature of the formation of intermetallic particles in repaired IN718 and an accurate analysis to determine the identity of these particles should be done, since the observation of this intermetallic is accomplished in this work together with a proposed complete examination of this intermetallic;

4) A high spark frequency with low pulse energy can be explored in a future project involving the repairing of Ni-based superalloy like IN718, since the quality of deposition in terms of internal defects and roughness may be affected by the energy input;

5) A deeper notch may be used to induce substantial differences in the tensile properties like yield stress, ultimate tensile stresses and ductility of repaired samples using ESD.

References

[1] Y. Xie and M. Wang, "Isothermal oxidation behavior of electrospark deposited MCrAIX-type coatings on a Ni-based superalloy," *Journal of Alloys and Compounds,* vol. 408, no. 2, pp. 454-461, 8 July 2009.

[2] S. Frangini and A. Masci, "A study on the effect of a dynamic contact force control for improving electrospark coating properties," *Surface and Coatings Technology,* vol. 204, no. 16-17, pp. 2613-2623, 15 May 2010.

[3] J. L. Reynolds Jr., R. L. Holdren and L. E. Brown, "Electro-Spark Deposition," *Advanced Materials & Processes,* vol. 61, no. 3, p. ASM International, 01 March 2003.

[4] J. Padgurskas, R. Kreivaitis, R. Rukuiža, V. Mihailov, V. Agafii, R. Kriūkienė and A. Baltušnikas, "Tribological properties of coatings obtained by electro-spark alloying C45 steel surfaces," *Surface and Coatings Technology,* vol. 311, pp. 90-97, 15 February 2017.

[5] E. Anisimov, A. K. Khan and O. A. Ojo, "Analysis of microstructure in electro-spark deposited N718 superalloy," *Materials Characterization,* vol. 119, p. 233–240, September 2016.

[6] K. Maciejewski, *The Role of Microstructure on Deformation and Damage Mechanisms in a Ni-based Superalloy at Elevated Temperatures,* Kingston: University of Rhode Island, 2013.

[7] T. M. Pollock and S. Tin, "Nickel-Based Superalloys for Advanced Turbine Engines: Chemistry, Microstructure, and Properties," *Journal of Propulsion and Power,* vol. 22, no. 2, pp. 361-374, 2006.

[8] S. Üzgür, Y. Uzunonat, S. F. Diltemiz and R. Gunay, "State-of-Art Technology ALLVAC 718 Plus Superalloy for Gas Turbine Engine Parts," *Advanced Materials Research,* vol. 213, pp. 131-135, 2011.

[9] S. Kim, Y. Hwang, T. Kim and C. Shu, "Failure analysis of J85 Engine turbine blades," *Engineering Failure Analysis,* vol. 15, no. 4, pp. 394-400, June 2008.

[10] Z. Khan, S. Fida, F. Nisar and N. Alam, "Investigation of Intergranular Corrosion in 2nd stage gas turbine blades of an aircraft engine," *Engineering Failure Analysis,* vol. 68, pp. 197-209, October 2016.

[11] X. Ye, X. Hua, M. Wang and S. Lou, "Controlling hot cracking in Ni-based Inconel-718 superalloy cast sheets during tungsten inert gas welding," *Journal of Materials Processing Technology,* vol. 222, pp. 381-390, August 2015.

[12] ASM International, ASM Specialty Handbook: Nickel, Cobalt, and Their Alloys, Russell Township, Ohio: ASM International, 2000.

[13] A. Gregori and D. Bertaso, "Welding and Deposition of Nickel Superalloys 718, Waspaloy and Single Crystal Alloy CMSX-10," *Welding in the World,* vol. 51, no. 11-12, p. 34–47, 2007.

[14] M. Brochu, J. G. Portillo, J. Milligan and D. W. Heard, "Development of Metastable Solidification Structures Using the Electrospark Deposition Process," *The Open Surface Science Journal,* vol. 3, pp. 105-114, 2011.

[15] R. N. Johnson and G. L. Sheldon, "Advances in the electrospark deposition coating process," *Journal of Vacuum Science & Technology A: Vacuum, Surfaces, and Films,* vol. 4, no. 6, p. 2740 – 2746, 1986.

[16] O. Sahin and A. V. Ribalko , "Electrospark Deposition: Mass Transfer," in *Mass Transfer - Advanced Aspects*, InTech, 2011.

[17] J. Liu, R. Wang and Y. Qian, "The formation of a single-pulse electrospark deposition spot," *Surface and Coatings Technology,* vol. 200, no. 7, p. 2433–2437, 21 December 2005.

[18] M. Ebrahimniaa, F. M. Ghainia, Y. J. Xieb and H. Shahverdia, "Microstructural characteristics of the built up layer of a precipitation hardened nickel based superalloy by electrospark deposition," *Surface and Coatings Technology,* vol. 258, pp. 515-523, 15 November 2014.

[19] S. K. Tang, *The Process Fundamentals and Parameters of Electro-Spark Deposition,* Waterloo, Ontario: University of Waterloo Thesis, 2009.

[20] P. V. Kiryukhantsev-Korneev, A. N. Sheveyko, N. V. Shvindina, E. A. Levashov and D. V. Shtansky, "Comparative study of Ti-C-Ni-Al, Ti-C-Ni-Fe, and Ti-C-Ni-Al/Ti-C-Ni-Fe coatings produced by magnetron sputtering, electro-spark deposition, and a combined two-step process," *Ceramics International,* vol. 44, no. 7, pp. 7637-7646, May 2018.

[21] W. Wang, M. Wang, F. Sun, Y. Zheng and J. Jiao, "Microstructure and cavitation erosion characteristics of Al–Si alloy coating prepared by electrospark deposition," *Surface and Coatings Technology,* vol. 201, no. 21, pp. 5116-5121, 30 July 2008.

[22] P. Leo, G. Renna and G. Casalino, "Study of the Direct Metal Deposition of AA2024 by ElectroSpark for Coating and Reparation Scopes," *Applied Sciences,* vol. 7, p. 945, 2017.

[23] D. W. Heard, "Rapid Solidification of an Aluminum-Lithium Alloy for Solid Freeform Fabrication Applications," Montreal, 2013.

[24] R. E. Smallman and A. H. Ngan, Physical Metallurgy and Advanced Materials, 7th ed., Oxford: Elsevier Ltd, 2007, p. 650.

[25] ASM International, ASM HANDBOOK Volume 09: Metallography and Microstructures, vol. 09, ASM International, 1998.

[26] P. Kratochvíl, V. Vodičková, R. Král and M. Švec, "The Effect of Laves Phase (Fe,Al)2Zr on the High-Temperature Strength of Carbon-Alloyed Fe3Al Aluminide," *Metallurgical and Materials Transactions A,* vol. 47, no. 3, p. 1128–1131, March 2016.

[27] Max-Planck-Institut für Eisenforschung GmbH, "Laves phases in the Fe- and Cr-based ternary systems Fe/Cr-Al-Nb," Max-Planck-Institut, [Online]. Available: https://www.mpie.de/3027439/laves_phases. [Accessed 09 November 2017].

[28] T. Kurzynowski, I. Smolina, K. Kobiela, B. Kuźnicka and E. Chlebus, "Wear and corrosion behaviour of Inconel 718 laser surface alloyed with rhenium," *Materials & Design,* vol. 132, pp. 349-359, 15 Otober 2017.

[29] M. Bambach, I. Sizova, F. Silze and M. Schnick, "Hot workability and microstructure evolution of the nickel-based superalloy Inconel 718 produced by laser metal deposition," *Journal of Alloys and Compounds,* vol. 740, pp. 278-287, 5 April 2018.

[30] H. C. Radhakrishna and K. Prasad Rao, "The formation and control of Laves phase in superalloy 718 welds," *Journal of Materials Science,* vol. 32, no. 8, p. 1977–1984, April 1997.

[31] H. Qi, M. Azer and A. Ritter, "Studies of Standard Heat Treatment Effects on Microstructure and Mechanical Properties of Laser Net Shape Manufactured INCONEL 718," *Metallurgical and Materials Transactions A,* vol. 40, no. 10, p. 2410–2422, 14 August 2009.

[32] G. D. Ram, A. V. Reddy, K. P. Rao and G. M. Reddy, "Control of Laves phase in Inconel 718 GTA welds," *Science and Technology of Welding and Joining,* vol. 9, no. 4, pp. 390-398, 04 December 2013.

[33] L. L. Parimi, G. A. Ravi , D. Clark and M. M. Attallah, "Microstructural and texture development in direct laser fabricated IN718," *Materials Characterization,* vol. 89, pp. 102-111, March 2014.

[34] Y. Chen, K. Zhang, J. Huang, S. R. E. Hosseini and Z. Li, "Characterization of heat affected zone liquation cracking in laser additive manufacturing of Inconel 718," *Materials & Design,* vol. 90, pp. 586-594, 15 January 2016.

[35] V. Champagne, M. Pepi and B. Edwards, "Defense Technical Information Center," July 2006. [Online]. Available: http://www.dtic.mil/docs/citations/ADA453366. [Accessed 28 September 2017].

[36] N. Radek and K. Bartkowiak, "Performance properties of electro-spark deposited carbide-ceramic coatings modified by laser beam," in *LANE 2010 - 6th International Conference on Laser Assisted Net Shape Engineering*, Erlangen, Germany, 2010.

[37] N. Radek and K. Bartkowiak, "Laser Treatment of Electro-Spark Coatings Deposited in the Carbon Steel Substrate with using Nanostructured WC-Cu Electrodes," in *LANE 2012 - 7th International Conference & Exhibition on Photonic Technologies*, Fürth, Germany , 2012.

[38] X. Wei, Z. Chen, J. Zhong and Y. Xiang, "Feasibility of preparing Mo2FeB2-based cermet coating by electrospark deposition on high speed steel," *Surface and Coatings Technology,* vol. 296, pp. 58-64, 26 June 2016.

[39] Q. Jing and Y. Tan, "Microstructure and Tribological Properties of Cobalt-based Stellite 6 Alloy Coating by Electro-Spark Deposition," *Materials Research,* vol. 16, no. 5, pp. 1071-1076, 28 May 2013.

[40] Y. Xie and M. Wang, "Microstructural morphology of electrospark deposition layer of a high gamma prime superalloy," *Surface and Coatings Technology,* vol. 201, no. 3-4, pp. 691-698, 5 October 2006.

[41] S. H. Baghjari, F. M. Ghaini, H. R. Shahverdi, M. Ebrahimnia, C. Mapelli and S. Barella, "Characteristics of electrospark deposition of a nickel-based alloy on 410 stainless steel for purpose of facilitating dissimilar metal welding by laser," *The International Journal of Advanced Manufacturing Technology,* vol. 97, no. 9-12, p. 2821–2828, December 2016.

[42] R. W. Messler Jr, Principles of Welding, Weinheim: WILEY-VCH, 2004.

[43] S. Durdu, S. L. Aktuğ and K. Korkmaz, "Characterization and mechanical properties of the duplex coatings produced on steel by electro-spark deposition and micro-arc oxidation," *Surface and Coatings Technology,* vol. 236, pp. 303-308, 15 December 2013.

[44] A. Lešnjak and J. Tušek, "Processes and properties of deposits in electrospark deposition," *Science and Technology of Welding and Joining,* vol. 7, no. 6, pp. 391-396, 2002.

[45] K. Korkmaz, "Investigation and characterization of electrospark deposited chromium carbide-based coating on the steel," *Surface and Coatings Technology,* vol. 272, pp. 1-7, 25 June 2015.

[46] J. Liang, W. Gao, Z. Li and Y. He, "Hot corrosion resistance of electrospark-deposited Al and Ni Cr coatings containing dispersed Y2O3 particles," *Materials Letters,* vol. 58, no. 26, pp. 3280-3284, October 2004.

[47] A. Carofalo, V. Dattoma, R. Nobile, F. Panella, G. Alfeo, A. Scialpi and G. Zanon, "Mechanical Characterization of a Nickel-based Superalloy Repaired using

MicroPlasma and ESD Technology," in *XXIII Italian Group of Fracture Meeting, IGF XXIII*, Favignana, Italy, 2015.

[48] I. V. Galinov and R. B. Luban, "Mass transfer trends during electrospark alloying," *Surface and Coatings Technology,* vol. 79, no. 1-3, pp. 9-18, February 1996.

[49] A. D. Thamer, M. H. Hafiz and B. S. Mahdi, "Mechanism of Building-Up Deposited Layer during Electro-Spark Deposition," *Journal of Surface Engineered Materials and Advanced Technology,* vol. 2, no. 4, pp. 258-263, October 2012.

[50] C. Luo, S. Dong, X. Xiong and N. Zhou, "Mass loss of copper alloy electrode during TiB2 coating by electrospark deposition," *Surface & Coatings Technology,* vol. 203, no. 22, pp. 3333-3337, 15 August 2009.

[51] Y. Mei, Y. Liu, C. Liu, C. Li, L. Yu, Q. Guo and H. Li, "Effect of base metal and welding speed on fusion zone microstructure and HAZ hot-cracking of electron-beam welded Inconel 718," *Materials & Design,* vol. 89, pp. 964-977, 5 January 2016.

[52] ASM International, ASM Handbook Volume 15: Casting, ASM International, 1998.

[53] K. Sivaprasad and G. S. S. Raman, "Influence of magnetic arc oscillation and current pulsing on fatigue behavior of alloy 718 TIG weldments," *Materials Science and Engineering: A,* vol. 448, no. 1-2, pp. 120-127, 17 March 2007.

[54] Y. Zhang, Z. Li, P. Nie and Y. Wu, "Effect of Heat Treatment on Niobium Segregation of Laser-Cladded IN718 Alloy Coating," *Metallurgical and Materials Transactions A,* vol. 44, no. 2, p. 708–716, February 2013.

[55] A. V. Ribalko, O. Sahin and K. Korkmaz, "A modified electrospark alloying method for low surface roughness," *Surface and Coatings Technology,* vol. 203, no. 23, pp. 3509-3515, 25 August 2009.

[56] A. V. Ribalko and O. Sahin, "The use of bipolar current pulses in electrospark alloying of metal surfaces," *Surface and Coatings Technology,* vol. 168, no. 2-3, pp. 129-135, 22 May 2003.

[57] M. Wang, W. Wang, Y. Xie and J. Zhang, "Electro-spark epitaxial deposition of NiCoCrAlYTa alloy on directionally solidified nickel-based superalloy," *Transactions of Nonferrous Metals Society of China,* vol. 20, no. 5, pp. 795-802, May 2010.

[58] S. Kou, Welding Metallurgy, Hoboken: John Wiley & Sons, 2003.

[59] B. Hassan and J. Corney, "Grain boundary precipitation in Inconel 718 and ATI 718Plus," *Materials Science and Technology,* vol. 33, no. 16, pp. 1879-1889, 7 June 2017.

[60] X. Gong, X. Wang, Z. Jones, K. Cooper, V. Cole and K. Chou, "CHARACTERIZATION OF MICROSTRUCTURE AND MECHANICAL PROPERTY OF INCONEL," in *International Manufacturing Science and Engineering Conference* , Charlotte, 2015.

[61] R. Qu, P. Zhang and Z. Zhang, "Notch Effect of Materials: Strengthening or Weakening?," *Journal of Materials Science & Technology,* vol. 30, no. 6, pp. 599-608, June 2014.

[62] T. L. Anderson, Fracture Mechanics, Boca raton: Taylor & Francis, 2005.

[63] D. Deng, R. L. Peng, H. Brodin and J. Moverare, "Microstructure and mechanical properties of Inconel 718 produced by selective laser melting: Sample orientation dependence and effects of post heat treatments," *Materials Science and Engineering: A,* vol. 713, pp. 294-306, 24 January 2018.